# Polarization Dependent Femtosecond Laser Microstructuring of Silicon

by

Hajar Al-Khazraji

Thesis submitted to the
Faculty of Graduate and Postdoctoral Studies
In partial fulfillment of the requirements
For the M.Sc. degree in
Physics

Physics
Faculty of Science
University of Ottawa

# Abstract

Microstructuring of silicon is performed to alter its optical and electrical properties for use in photonic devices. Femtosecond lasers are a favourable structuring tool because they are extremely precise due to the confinement of their interaction to the focal volume. Experiments were carried out on N-type, P-type, and intrinsic silicon with a femtosecond laser operating at 800 nm, with pulse duration of 40 fs, and 1 kHz repetition rate. A single pulse produced a micro-ring structure surrounding a crater. It is caused by the motion of material according to the pressure gradient induced by the Gaussian profile of the laser. Multiple-pulse structures were similar to the single pulse except for the central protrusion of material. Two factors are responsible for multiple-pulse structures: (1) geometrical difference of the plasma compared to the single pulse (2) reflections of shockwaves produce protruding structures. Polarization dependence of all structures was observed.

**En français**:
Microstructure de silicium est effectuée pour modifier les propriétés optiques et électriques pour utilisation dans des dispositifs photoniques. Les lasers femtoseconde sont un outil de structuration favorable parce qu'ils sont extrêmement précis en raison de l'isolement de leur interaction au volume focale. Les expériences ont été réalisées sur de type N, type P, et le silicium intrinsèque avec un laser femtoseconde fonctionnant à 800 nm, avec une durée d'impulsion de 40 fs et une fréquence de répétition d'kHz. Une impulsion unique produit une structure de micro-anneau entourant un cratère. Il est provoqué par le mouvement du matériau en fonction du gradient de pression induit par le profil gaussien du laser. Structures multi-impulsions étaient semblables à l'impulsion unique, sauf pour la saillie centrale du matériau. Deux facteurs sont responsables de structures multi-impulsions: (1) la différence géométrique du plasma par rapport à l'impulsion unique (2) de réflexions des ondes de choc produites structures saillantes. La dépendance à la polarisation de l'ensemble des structures a été observée.

**Acknowledgements**

I would like to thank my supervisor Prof. Ravi Bhardwaj for aiding in the completion of this thesis. Special thanks is given to the PDF Deepak Kallepalli for participating in very fruitful discussions, as well as always being willing to explain everything to the best of his knowledge.

# Contents

# List of Figures

# Chapter 1

# Introduction

## 1.1 Motivation

This thesis is focused on studying femtosecond laser induced modification of silicon. Microstructuring is a technique used to manipulate the optical, electrical, chemical, and physical properties of a material so that it can be used in many applications ranging from micro-optical devices to bio-chemical sensors. Silicon is a commonly used material in these devices because of its small band-gap. It is an important property for building optical devices since it permits a range of wavelengths to be transmitted. This is useful for building waveguides and for manipulating nonlinear processes. Modification of silicon can occur via many routes and processes. Therefore, there are many possibilities of changes that can occur as a consequence of the laser impinging onto the surface. The hydrophobicity can change by structuring the surface [5, 6], and chemical properties of a material can also change, possibly due to laser assisted reactions [7, 8]. Mechanical properties such as durability, roughness or lustre, malleability, ductility, etc., may also become modified, rendering silicon useless in some industrial applications [9]. The band-gap can be decreased by doping, resulting in a substantial increase in absorption, which has applications in solar cells [10].

The purpose of this research is to develop structuring techniques through the understanding of the fundamental interactions between the laser and the material. For instance, knowing what properties have changed and how the structural modifications depend on the laser parameters are important for creating controlled modification techniques. The route we have taken entails systematically studying the single pulse structures first and then studying the structures formed by subsequent pulses.

## 1.2 Interaction of a femtosecond laser with a solid

Femtosecond lasers are used for material processing because their high intensities and short pulses allow for precise material structuring. When the photon energy is less than the band-gap of the material the light-matter interaction can be nonlinear [11]. At high enough intensities nonlinear absorption of light by electrons dominates over single photon absorption. Such a nonlinear process confines the interaction to the focal volume of the laser, since here the probability of the multiphoton absorption is the highest [12]. In addition, pulse durations of femtosecond lasers are shorter than the electron relaxation and heat conduction times so during the pulse the energy that is deposited is confined to the interaction volume. These two unique features of femtosecond lasers enable sub-micron precision of the fabricated structures.

When a femtosecond pulse impinges onto a solid, the first step of interaction is the excitation of electrons from the valence band to the conduction band. If the band-gap of the material is larger than the photon energy, electrons must be first ionized through multiphoton ionization MPI to become promoted. Once in the conduction band they promote other valence electrons by transfer of energy through inelastic collisions, the repetitive process of ionization and collisions is called avalanche ionization. Ionization of material occurs on the order of a femtosecond. The ionized electrons continue absorbing energy from the field through inverse Bremsstrahlung. After the end of the pulse electrons transfer their energy to the lattice via inelastic electron-phonon and electron-ion collisions on a picosecond timescale. On a nansecond timescale the energy transferred to the lattice leads to melting and/or material removal depending on the intensity of the pulse. Following melting the lattice reaches thermal equilibrium and the material re-solidifies on a longer timescale. In the following these key processes are described in detail.

### 1.2.1 Multiphoton ionization

Multiphoton ionization MPI occurs by the simultaneous absorption of two or more photons by a valence electron, causing it to enter into the conduction band. Figure 1.1 is a schematic showing how the energy of the absorbed photon (colour of arrow) decreases from linear to two to three photon absorption. The lower the energy of the photon the greater is the number of photons needed to reach the conduction band [12]. MPI requires a very intense pulse because the cross sections of two, three, etc. photon absorptions are much smaller than for a single photon. Therefore, the more intense the beam, the greater is the probability that two or more photons will be simultaneously in the vicinity of an

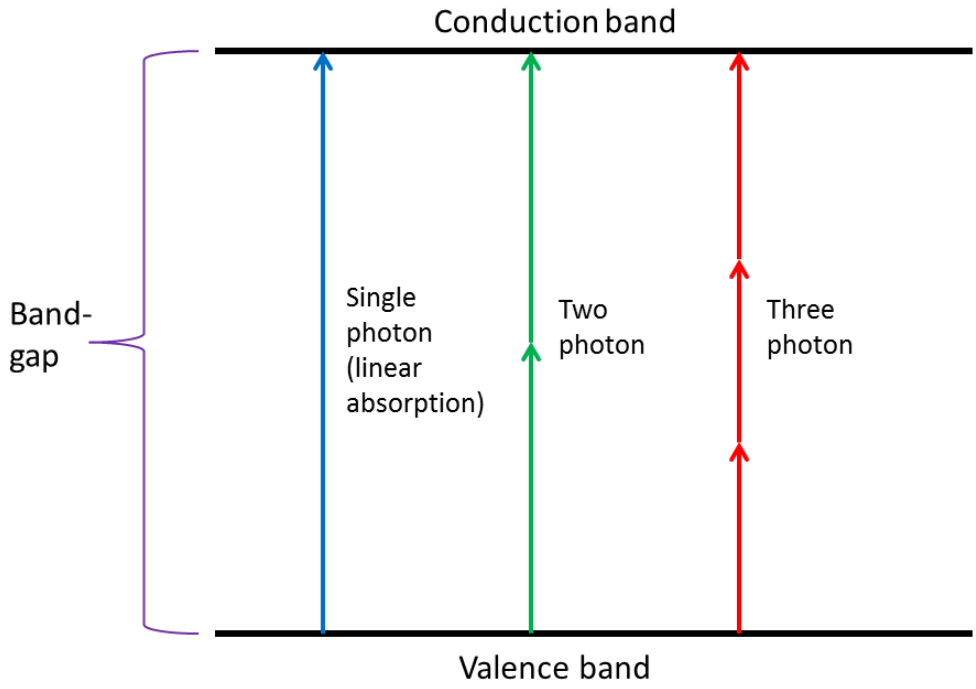


Figure 1.1: Linear and nonlinear absorption. As the photon energy is decreased, there is a greater number of photons required to excite the electrons to the conduction band. The energy of the photon is represented by the colour of the arrows.

electron. The probability per unit time $w_{mpi}$ of multiphoton ionization is proportional to:

$$w_{mpi} \ \alpha \ \sigma_n I^n \tag{1.1}$$

$\sigma_n$ is the cross section for simultaneous absorption of n photons, $I^n$ is the intensity of the pulse raised to the power of the number of photons required to ionize an electron. For the case of silicon with a band-gap of 1.1 eV, an 800 nm laser will be primarily absorbed linearly. However with a femtosecond pulse duration the intensity will be around $10^{13} - 10^{14} W/cm^2$ which is high enough to make the two photon cross section significant. In [13] the two photon absorption cross section is cited to be 9 cm/GW.

### 1.2.2 Collisional ionization

As electrons become ionized they are colliding with each other and nearby ions as well as scattering phonons. Some of these collisions help to ionize more electrons and make them eventually reach equilibrium. The collision rates will now briefly be discussed fol-

lowed by a discussion on avalanche ionization. When the electron temperature $T_e$ is less than the Fermi temperature $T_F$ the collision rate increases, and in this low temperature range the laser frequency is greater than the collision rate. The rate is dominated by electron-phonon collisions and thus is on the order of the phonon frequency of a THz. The maximum collision rate occurs when the electron temperature equals the Fermi temperature, and the electron energy approaches the ionization potential. At this temperature the solid has become a plasma hence the rate is nearly equal to the plasma frequency $\nu_{eff} \approx \omega_p >> \omega$ which is much greater than the laser frequency [14].

Avalanche ionization can be understood in the following way: (1) electrons oscillate in the presence of an electric field, and (2) they will transfer energy to other electrons through collisions. Those valence electrons that have gained energy greater than the band-gap through multiphoton absorption have entered into the conduction band are known as seeds. Each seed can in turn collide with a valence electron and transfer sufficient energy to it so that it also gets promoted to the conduction band. However in order for the seeds to promote other electrons and still be energetic enough to remain in the conduction band, they need to gain at least twice the band-gap energy from the field [11, 12, 14]. Figure 1.2 shows a schematic of collisional ionization. The repeated process of electrons gaining energy from the field, entering into the conduction band, and then promoting other valence electrons is known as avalanche ionization. Figure 1.2 shows one collision of this type that results in the promotion of a valence electron (green) and the simultaneous de-excitation of a conduction electron (blue). The probability per unit time of ionization by this process $w_{imp}$ is estimated by considering the energy gained by one electron [14]

$$w_{imp} \approx \frac{1}{\Delta_{gap}} \frac{d\epsilon"}{dt} \tag{1.2}$$

$\Delta_{gap}$ is the energy required to promote an electron from the top of the valence band to the bottom of the conduction band, and $\frac{d\epsilon"}{dt}$ is the rate of change of the dielectric function of the electron over time. The rate of change depends on the frequency of collisions as well as the frequency of oscillation of the electrons in the conduction band, or the quiver energy $\epsilon_{osc}$ [14]

$$\frac{d\epsilon"}{dt} = 2\epsilon_{osc} \frac{\omega^2 \nu_{eff}}{\nu_{eff}^2 + \omega^2}. \tag{1.3}$$

$\nu_{eff}$ is the effective collision frequency that includes contributions from both electron-ion and electron-phonon elastic collisions. The energy of the oscillating electron is known as

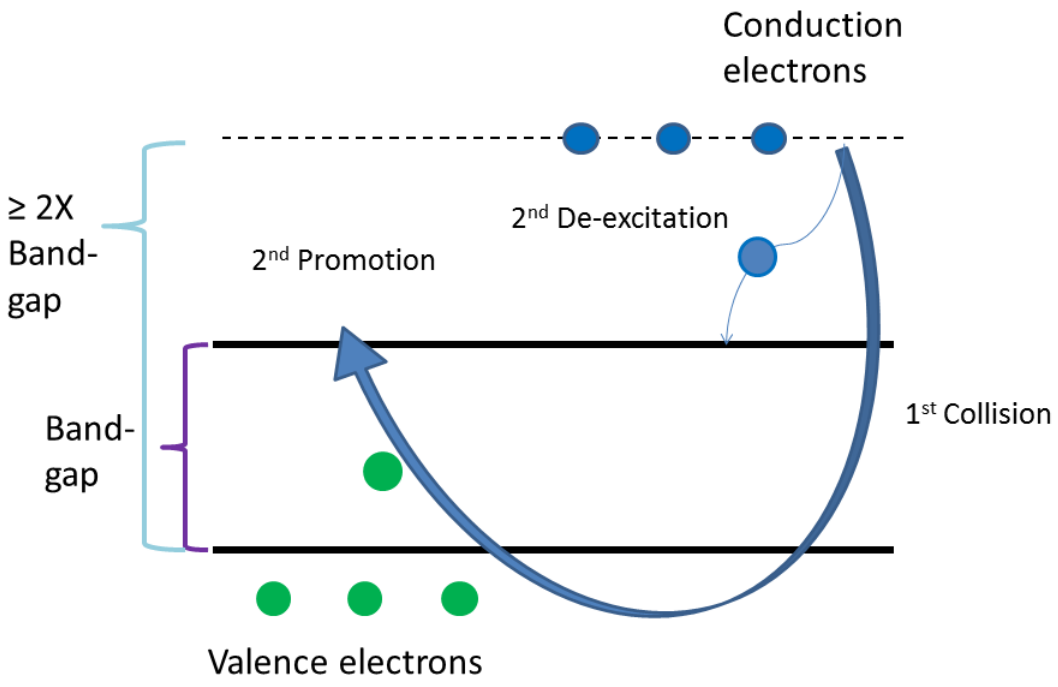


Figure 1.2: Process of avalanche ionization. Conduction electrons (blue) collide with valence electrons (green), and promote electrons from the valence band to the conduction band.

the quiver energy and has the form [14]

$$\epsilon_{osc} = 9.3(1+\alpha^2)\frac{I}{10^{14}}\lambda^2 \tag{1.4}$$

$\alpha$ is the elliptical parameter that varies from 0 (linearly polarized) to 1 (circularly polarized), I is the intensity in $W/cm^2$, and $\lambda$ is the wavelength of the laser in $\mu$m. During a time t there will be m=$w_{imp}$t avalanche ionizations. To determine how many electrons will be excited first consider that there was a valence electron which gained enough energy (through MPI) to enter into the conduction band. Then it promotes another electron resulting in the addition of two electrons to the band. Subsequently, each of these electrons will gain energy from the field and promote two more electrons resulting in four additional electrons. These four will gain energy and promote four more, resulting in a total of eight added electrons. Therefore avalanche ionization during a time t will result in the promotion of $2^m$ electrons. The remainder of the pulse after ionization

is absorbed by the ionized electrons through inverse bremsstrahlung; an electron in an external electric field will absorb energy as it scatters from the Coulomb field of nearby ions [12].

### 1.2.3 Plasma formation

During the leading edge of the pulse the laser energy is used to ionize the material, thus forming a plasma, and the remainder of the pulse interacts with this plasma. The electron equilibration time is about $10^{-2} fs$ for a plasma density of $10^{23} cm^{-3}$, which is substantially shorter than the pulse duration. Therefore, equilibrium is reached by the plasma, and the electron energy distribution follows the laser intensity profile for the remainder of the pulse [11]. The frequency of the plasma is the collective oscillation of the electrons composing it; it is the inverse of the time for collective motion [11]. In the following paragraphs, the interaction of the plasma with the remainder of the pulse will be briefly discussed. It is assumed that the electronic motion resembles that of an electron on a spring.

The differential equation describing the system of the electrons is [15]:

$$\frac{d^2x}{dt^2} - \omega^2 x = -eE(t)/m, \tag{1.5}$$

the right hand side is the driving force applied by the electric field of the laser, the first term on the left hand side is the acceleration of the electron, and the second term is the restoring spring force. Once the differential equation is solved for the position x, the susceptibility $\chi$ is retrieved by substituting x into the polarization equation:

$$P(t) = ex(t) = \epsilon_0 \chi E(t), \tag{1.6}$$

and isolating for $\chi$ [15]:

$$\chi = \frac{n\frac{e^2}{m}(\omega_0^2 - \omega^2)}{\epsilon_0[(\omega_0^2 - \omega^2)^2 + 4\omega_\gamma^2]} + \frac{in\frac{e^2}{m}2\omega_\gamma}{\epsilon_0[(\omega_0^2 - \omega^2)^2 + 4\omega_\gamma^2]}. \tag{1.7}$$

n is the electron density, $\omega_0$ is the laser frequency, $\omega$ is the plasma frequency, $\omega_\gamma$ is the full width at half maximum of the state. As usual e is the fundamental charge of an electron, m is its mass, and $\epsilon_0$ is the permittivity in vacuum. The response of the plasma can be quantified by $\chi$ since the permittivity and thus index of refraction are defined through $\chi$:

$$n = \sqrt{\epsilon} = \sqrt{1 + \chi}. \tag{1.8}$$

When the plasma oscillates with the laser frequency, the real part of $\chi$ vanishes. The laser frequency is the resonant frequency of the plasma, which is the critical frequency. At this frequency there is a substantial absorption of laser light by the plasma, and this is explained by the vanishing of the real part. Below the critical frequency the real part is large and the imaginary part is small; the laser is able to propagate through the plasma with little attenuation. Above the critical frequency the real part is large and negative with a small imaginary part; the laser is reflected upon incidence with little absorption.

The plasma frequency is related to electron density by:

$$\omega = \sqrt{\frac{ne^2}{\epsilon m}}, \tag{1.9}$$

with n being electron density and m being the mass of an electron. According to this equation for a fixed effective mass and permittivity, the frequency of oscillation is greater for a high density than a low density plasma. Overdense plasmas have densities greater than the critical density and thus oscillate above the critical frequency, underdense plasmas have densities below and oscillate below the critical value.

### 1.2.4 Lattice heating and relaxation

After the end of the pulse there are relaxation processes that occur before the laser-solid system reaches equilibrium. Equilibration for electron and phonon subsystems is reached within several tens of femtoseconds after the pulse is incident [14] when the lattice temperature is much less than the electron temperature $T_l << T_e$. The time required for electrons to transfer their energy to the lattice is on the order of picoseconds. As the electrons transfer heat to the lattice shielding becomes more important and single particle influences are no longer considered. The temperature for considering group interactions is known as the Debye temperature. When the lattice temperature is around the Debye temperature $T_D$ phonon-phonon collisions occur at a rate that is proportional to the phonon frequency. The phonon subsystem develops a Bose-Einstein distribution when it establishes equilibrium. At the Fermi level the electron-ion collision rate is much lower than the electron-phonon rate. This is because the great difference between the electron and ion temperatures results in screening that ultimately decreases their collision rate. However, the electron-ion collision rate is heavily influenced by electron temperature, because the increasing electron temperature makes the Coulomb collisions more significant. The electron-ion energy transfer takes around 12 ps; about one order of magnitude longer than the electron-phonon system [14].

For a medium with a band-gap that is smaller than the energy of the incident laser, the interaction with the solid will take place within the skin depth. The skin depth is the depth travelled by the laser to reduce its intensity by a factor of $1/e^2$. The decrease in electric field depends exponentially on the depth x [11]:

$$E(x) = E(0)e^{\frac{-x}{l_s}} \tag{1.10}$$

with the skin depth being defined as:

$$l_s = \frac{c}{\omega k} \tag{1.11}$$

k is the imaginary part of the refractive index, c is the speed of light, and $\omega$ is the laser frequency. The loss of intensity is due to absorption by various processes such as electron excitation, ionization, as well as absorption by defects and impurities.

Heat conduction by transport of electrons is the primary mode of conducting heat through the sample. The amount of energy density deposited per unit time $Q_{e-th}$ depends on the gradient of electronic temperature $\nabla T_e$ and the electronic heat conduction coefficient $\kappa_e$ [14]:

$$Q_{e-th} = \kappa_e \nabla T_e. \tag{1.12}$$

$\kappa_e$ $\left[\frac{W}{cmK}\right]$ depends on the mean free path $l_e$ of colliding electrons, which inversely depends on the momentum transfer to the electrons from collisions with phonons: $l_e = v_e/\nu_{e-ph}^{mom}$, with $v_e$ being the average velocity of electrons. Time for spreading the heat across the skin depth by the diffusion of electrons is:

$$t_{heat} = l_s^2/D_{diff}, \tag{1.13}$$

$l_{abs}$ is the skin depth and $D_{diff}[cm^2/\mathrm{s}]$ is the diffusion coefficient. According to this formula heat conduction occurs on the tens of picoseconds timescale. Electron-phonon momentum transfer rate dominates the heat diffusion. Heat conduction by the diffusion of electrons is valid when the mean free path is substantially shorter than the heat length.

### 1.2.5 Comparison with longer pulses

Electron relaxation times for femtosecond pulses are greater than the pulse duration, and are on the order of 1 ps. Femtosecond pulses with intensities in the range of $10^{13} - 10^{14} W/cm^2$ nearly completely ionize any material. Therefore all of the absorbed energy during the pulse is going to the thermal energy of the electrons, the lattice temperature remains the same, and there is no thermal expansion of the solid [12]. On the

other hand, for longer pulses such as pico and nanosecond pulses, the electron-lattice energy transfer time is approximately equal to the pulse duration. Therefore, the electron and ion temperatures become equal near the starting of the pulse, hence the lattice temperature increases during the pulse and thermal expansion occurs [16]. Heat conduction and hydrodynamic expansion become the main processes that drive ablation. For femtosecond pulses the laser energy is absorbed by electrons and is primarily used to ionize the material via avalanche and multiphoton ionization. For longer pulses the absorbed energy is not used towards generating a high density plasma since the intensity is too low to substantially ionize the material. Instead, the absorbed energy is used to break bonds during the pulse. For long pulses absorption is small and is primarily due to defects and some interband transitions before equilibrium is reached between the ions and electrons [11]. Figure 1.3 shows the differences between the craters formed using $10^4$ femtosecond pulses (right image) versus $10^4$ picosecond pulses (left image) [17]. Both ablations were made on steel with 200 fs and 80 ps pulses with energies 120 $\mu$J and 900 $\mu$J energies respectively. It is clear that the structure produced with the femtosecond laser is much smoother and cleaner than the picosecond pulse.

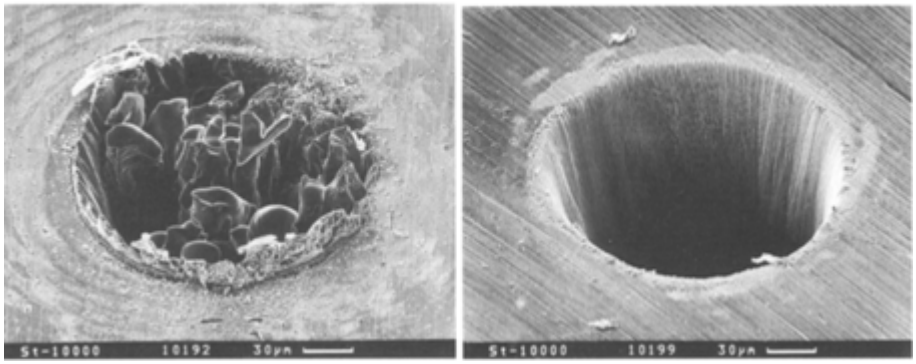


Figure 1.3: Comparison of femtosecond to picosecond pulses on steel with $10^4$ pulses [17].

Femtosecond pulses offer greater precision to micromachining than picosecond pulses. The high intensities of femtosecond pulses $10^{13} - 10^{14} W/cm^2$ coupled with the short durations give femtosecond pulses their trademark precision over longer pulses. High intensities increase the probability of nonlinear absorption, which allows the modified region to be restricted to the focus of the laser. Also, the time required for the electron temperature within the skin depth to become constant is much longer than the pulse duration, thus heat conduction does not affect the lattice during the pulse. Unlike

picosecond pulses, femtosecond pulses are shorter than the electron relaxation time, which means during the pulse there is no modification of the material density nor the ablated material. Thus, the timescales and intensities of femtosecond lasers give them the properties to be efficient structuring tools.

## 1.3 Overview of previous related work

Laser ablation by femtosecond pulses has been used to structure the surface of silicon to create laser induced periodic surface structures (LIPSS) or ripples and periodic arrays of conical spikes. LIPSS are periodic patterns that have spatial periods that are related to the laser wavelength. They were first discovered by irradiating transparent materials with picosecond lasers near the melting threshold of the material. Around the time of the late seventies and early eighties these ripples were also discovered to occur on silicon [18] [19]. The morphology after irradiation of transparent media and silicon with many lasers of various pulse durations was similar.

Single pulse experiments were performed and ripples were found only in the regions where the fluence was near the melting threshold. The period of the ripples formed was similar to the wavelength of the laser. Ripple formation was immediately connected to non-uniform melting and the notion of heterogeneous fluctuations in the damage mechanism. During the mid-eighties a theory was developed by considering how a linearly polarized pulse will interact with a surface. A pulse impinging on a surface that is microscopically rough will produce scattered waves that in turn will interfere with the incident wave which results in inhomogeneous absorption [20]. This produces an inhomogeneous melt thickness in which the interfering waves freeze in place thus imprinting ripples on the surface. In [18] the process of formation of ripples was studied. Experiments involving the irradiation of thin samples of silicon were performed with 38 ps pulses centred at 1.06 $\mu$m produced by an Nd:YAG laser. The morphology was studied using linearly polarized light focused on a silicon wafer ((111) or (100)) with an exposed area of 0.5 $cm^2$. SEM images were used to examine the ripples. In order to probe how the damage was formed, the transmission of the thin sample was measured during the experiment by a continuous wave He-Ne laser. Changes in the transmitted intensity over time were recorded and it was found that at a certain irradiation intensity of the Nd:YAG laser the transmission followed a sigmoid, which is indicative of a nucleation and growth evolution. Thus authors of [18] explained ripple formation in the context of damage kinetics where the processes of nucleation and then growth shape the morphology of the material

after irradiation. In [19] irradiations were performed on silicon and gallium arsenide with Gaussian pulses produced by a Nd:YAG laser centred at 532 nm with a pulse duration of 80 ps. The focal spot was between 40 $\mu$m and 300 $\mu$m. It was found, after a single pulse irradiation, that the central portion of the beam melted the surface and there was a transition from amorphous in the centre to polycrystalline at the outskirts. Between the fluence regions of 250 mJ/$cm^2$ in the centre and 100 mJ/$cm^2$ in the annular region, ripples form within this distinct fluence range. The authors of [19] observed LIPSS after single and multiple pulse irradiations. For single and multiple pulses they found that ripples formed perpendicular to the direction of the electric field. By changing the angle of incidence for p-polarized pulses the spatial period $\Lambda$ of the ripples changed according to:

$$\Lambda = \frac{\lambda}{1 \pm sin\theta}, \tag{1.14}$$

with $\lambda$ being the laser wavelength and $\theta$ being the angle of incidence. For s-polarized pulses the period was equal to $\lambda$. Many other experiments have been performed using linearly polarized light and the orientation of the ripples depended on the orientation of the field. For instance, Figure 1.4 is an example of the more recent work that demonstrates that the orientation of the ripples changed from being perpendicular in the high fluence region to parallel in the low fluence. Also, the frequencies of the ripples depend on the fluence; high frequency for low fluence and low frequency for high fluence. Figure 1.4 shows silicon (100) after irradiation with 350 pulses by a 2100 nm, 50 fs laser [1]. The pulses were focused using a 150 mm lens that focused the light to an area with a diameter 40 - 70 $\mu$m.

More recently, LIPSS have been observed for circularly polarized light in ablation experiments [21]. The experiments in [21] were performed using 100 fs pulses centred at 800 nm from a Ti:sapphire laser operating at 1 kHz. Silicon was irradiated by multiple pulses with fluences around the ablation threshold. Craters produced by ablation contained many types of patterns such as linear arrays of spherical nanoparticles, and regions of randomly oriented long lines with bifurcations. The traditional theory of inhomogeneous absorption to explain the patterns is not used to explain these observations. Instead a theory based on self-organization after surface instabilities [22] is used. In materials with strong coupling between electrons and phonons such as semiconductors, electrons become excited upon absorption of femtosecond pulses, hence the strong coupling inflicts a destabilization of the lattice. Since electron-phonon collisions relax on the order of a picosecond, the instability of the lattice occurs on the same timescale [22] [23]. The model explaining how self-organization is the origin of surface patterning is based on

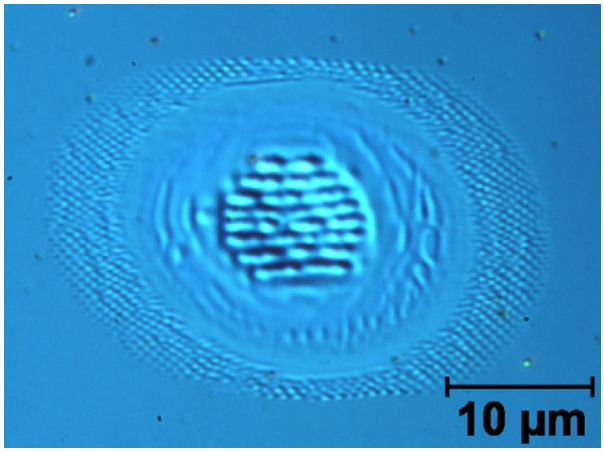


Figure 1.4: LIPSS formed on silicon [1]

the assumption that the generation of ions colliding in the material establish a collisional cascade and a random deceleration of particles. The cascade and random deceleration acts as a perturbation. It creates different diffusion rates in the material which acts to modulate the surface and thus ripples are formed.

Multiple-shot irradiation of silicon by femtosecond pulses with fluences above the ablation threshold created arrays of conical spikes when irradiation was performed in a halogen containing atmosphere [2]. These periodic cones were first observed in 1998 [2]. They used N-type Si(100) wafers with resistivity near $5 * 10^{-5} \Omega m$ in an atmosphere with 500 Torr $Cl_2$, $SF_6$, $N_2$, or $He_2$. Figure 1.5 shows the quasi-periodic array of cones created on the surface of silicon in $SF_6$ gas after irradiating the surface with 500 laser pulses with durations of 100 fs. The wafers were irradiated at normal incidence using a 10cm focal length lens with a spot size of 200 $\mu$m and a fluence of $10 J/cm^2$; much greater than the single pulse ablation threshold of 0.3 $J/cm^2$. The sample was placed on a stage and each spot received 500 pulses. The high aspect ratio characteristic of the cones is lost when the irradiation is performed under vacuum; instead the conical structures are blunter. The halogen gas such as sulfur hexafluoride can be dissociated by the laser, and the fluoride radical can etch silicon by forming silicon tetrafluoride. Later, the bandgap of silicon was modified by doping it with sulfur so that it would absorb nearly all of the incident light: UV, VI, NIR, etc. This increase of absorption was exploited to create IR photodetectors and eventually for use in solar cells [10].

The formation of periodic surface structures and conical spikes employed lenses that

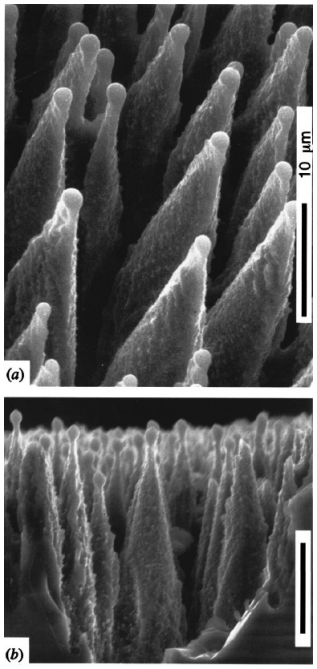


Figure 1.5: Cones formed on silicon after hundreds of pulses [2]

focused the laser to a diameter of several tens to a couple of hundreds of microns. In our study we draw attention to structuring the surface of silicon with lenses that focus the beam to less than 4 microns. Changing the size of the focal spot changes the steepness of the intensity gradient according to:

$$I(r,t) = I_0(r,t)e^{-2r^2/w_0^2}, \tag{1.15}$$

where I is the intensity and $w_0$ is the beam radius at the focus. For instance, the beams with the diameters used in the previously mentioned experiments have distinct regions of ablation and melting since the decay of the intensity is slower [24]. The consequence of a slower decay is a microscopically visible spatial transition between the different processes that depend on fluence, such as ablation and melting. Figure 1.4 is an example of how the different processes can be visible for large spot sizes. In the centre is the high fluence regime that results in the low frequency LIPSS and the surrounding ring of low fluence produces high frequency LIPSS. However for tightly focused beams such as the beam used in [25], the intensity gradient is so sharp that if the central portion of the beam ablated the material, there was a negligible portion that melted it. In reference [25] the focal diameter was 6.7 microns; much smaller than the diameters used in the previously

mentioned experiments. It is hypothesized that our results will more closely resemble the results of [25] than the others. With a diameter of 6.7 microns they observed smooth craters surrounded by raised rings for energies less than 300 nJ and for higher energies there was an explosive removal of material. Since our study will employ a lens with a smaller focal area, we expect the structure to also be smooth with a ring but smaller and less deep for the same energy range as a consequence of the tighter focusing.

In addition to exploring the structure produced by tight focusing, polarization dependence was also explored. Since silicon is a small band-gap material a high density plasma will be formed upon ionization. Polarization effects linked to under and overcritical plasma densities have been observed in PMMA [26], and are likely to exist in our study. Therefore, a thorough investigation of the effects of changing the orientations of linear and elliptical polarizations needed to be performed.

# Chapter 2

# Experimental methods and setup

## 2.1 Experimental procedure

The laser system used in our experiments is a Ti-sapphire regenerative amplifier from Spectra Physics that produces 40 fs pulses centred at 800 nm at a repetition rate of 1 kHz, and a maximum pulse energy of 2 mJ. The oscillator provided the seed pulse to the amplifier at a repetition rate of 76 MHz. The seed pulse energy is 8 nJ with a duration of 30 fs.

N-type doped with phosphorus, P-type doped with boron, and intrinsic silicon (100) wafers with resistivities in the range of $1 - 100\Omega m$ were used for structuring. The fluences used varied from about $0.1 - 5J/cm^2$. Single pulse experiments were performed on all three types but multiple-pulse experiments of up to five pulses were performed only on N-type. Pulses were administered using a LabView program that controls triggering the Pockels cells; multiple pulses were separated by the repetition rate of the laser. After each pulse the stage was moved in the x direction 10 microns to prevent overlapping of the pulses. Polarization dependence of single and multiple-pulse structures was investigated by placing either a half wave or quarter wave plate after the cube beam polarizer.

Figures 2.1 and 2.2 show the beam delivery optics directing the beam to the sample. In Figure 2.1 a beam sampler reflects a small portion of the amplifier output into the autocorrelator for continuous monitoring of the pulse duration. The transmitted beam propagates through a combination of half wave plate mounted onto a computer controlled rotation stage and a polarizer to change the pulse energy.

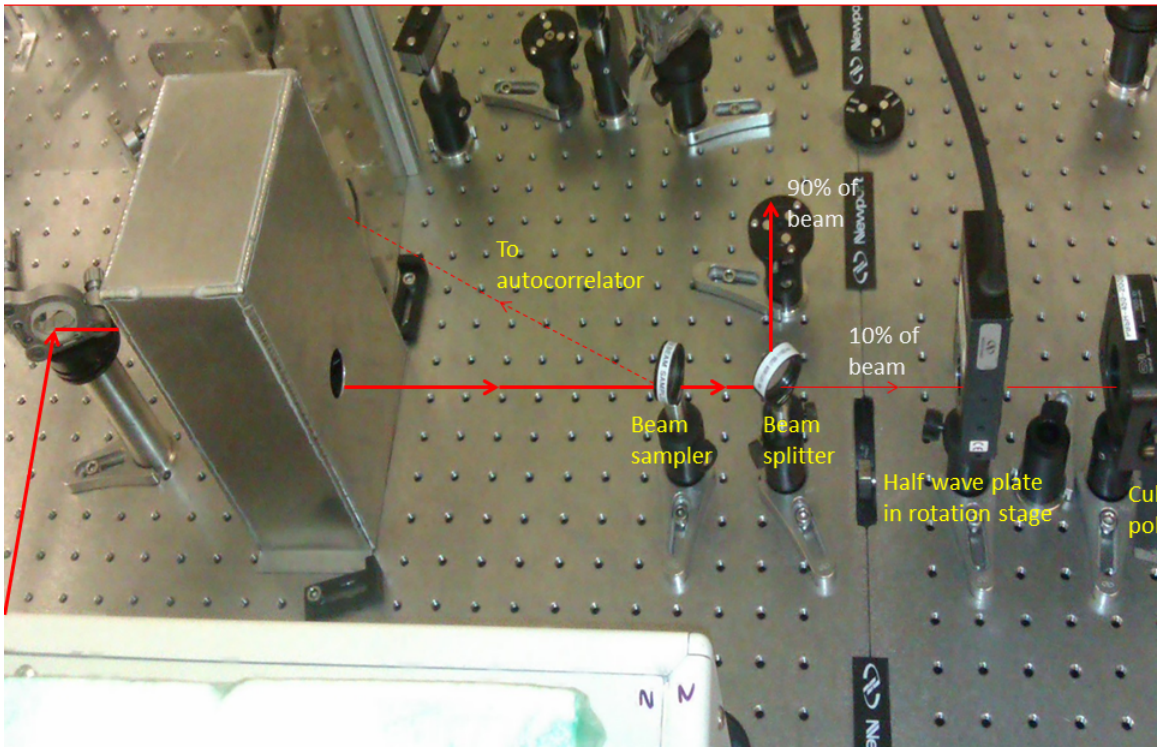


Figure 2.1: The output of the amplifier is reflected into the metallic box that contains a periscope to lower the beam closer to the optics table. The beam sampler reflects a portion to the autocorrelator and the remainder through the beam splitter, half wave plate, and cube beam polarizer.

After passing through a shutter, shown in Figure 2.2, the beam is directed vertically into an aperture. Then the beam is reflected down into a 16X microscope objective lens with NA 0.25 that focuses the laser beam onto the sample. The sample is placed on an xyz translation stage with a precision of 100 nm in x and y directions and 200 nm in the z direction. Alignment of the setup is checked by placing an IR card after the objective lens and observing the beam spot. There should appear a full circle that is concentric with an outer ring. This pattern is caused by the Airy disc intensity distribution of the focused light.

The sample surface is accurately determined by directing the light (with a glass slide) that has reflected from the surface and propagated through the microscope objective

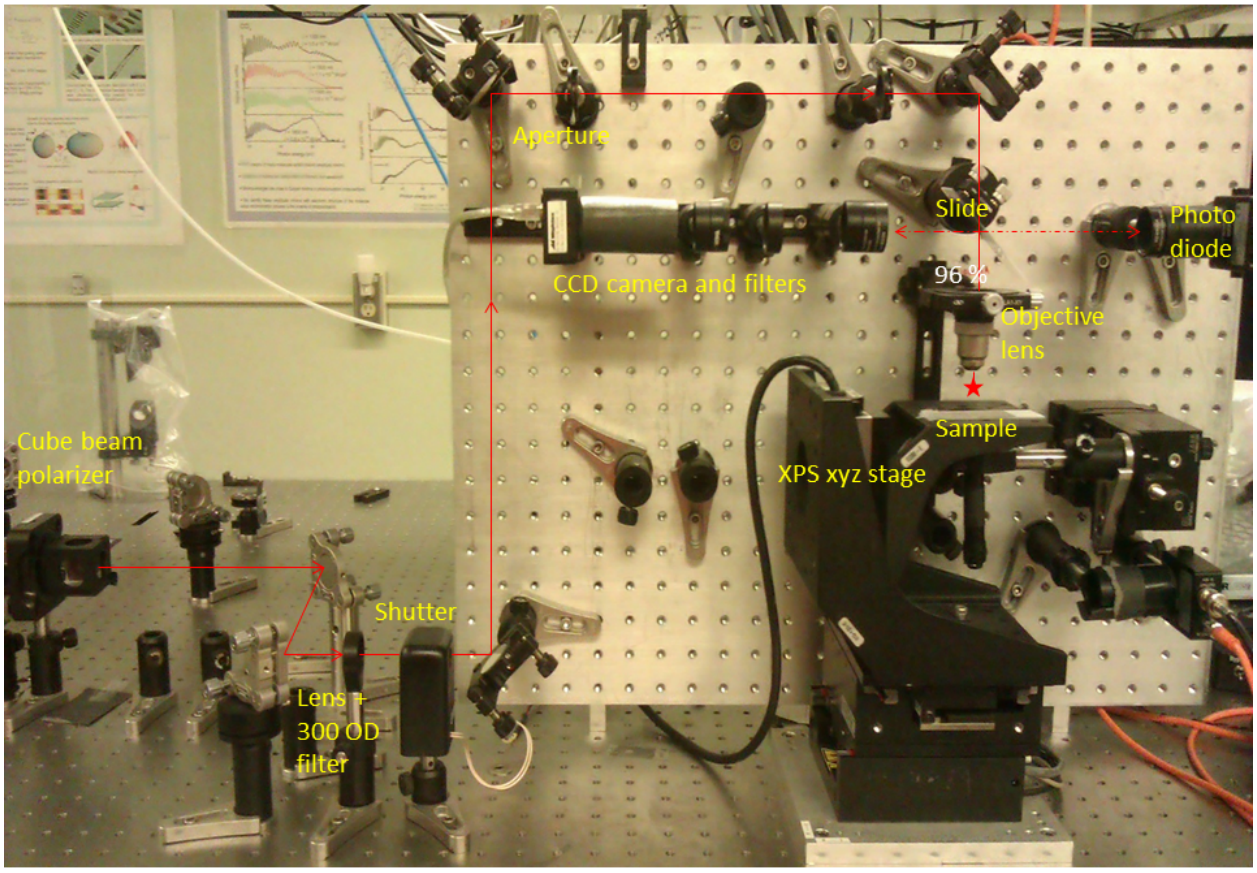


Figure 2.2: Continuation of Figure 2.1, p-polarized light is reflected by a pair of mirrors through a 300 OD filter followed by a shutter. The beam is reflected upward to go through a series of mirrors and apertures which direct the beam into the objective. The glass slide is placed to reflect less than 4 % to the CCD camera. The sample is placed on the stage.

into an imaging setup consisting of a lens and a camera (Figure 2.2). A series of neutral density filters were placed before the camera to ensure the intensity of the focused light was below the damage threshold of the camera. In order to find the surface safely, the energy of the incident beam was reduced to the lowest energy by changing the angle of the half wave plate according to the energy calibration discussed in the next subsection. A software to operate the camera was used to view the sample surface. The sample height was adjusted until two, sharp spots appeared on the screen. Each spot corresponded to

the reflection at the two air-glass interfaces of the glass slide used to reflect the beam into the camera. The accuracy of the sample surface is determined by the Rayleigh range (eq. 2.2). For the 16X lens the Rayleigh range is 11 $\mu$m, thus the surface is found within approximately a few microns.

### 2.1.1 Energy calibration

The energy was controlled with a half wave plate and cube beam polarizer combination so that rotation of the plate changed the polarization and hence the magnitude of the transmitted component. In this setup the orientation of the electric field was parallel to the optics table and parallel to the half wave plate crystal. The polarizer was oriented so that the cosine of the angle between the fields entering and exiting the wave plate, was the component of the electric field that was transmitted by the polarizer. Energy and half wave plate angle calibration curves were collected at the start of each experiment to account for day to day instabilities. The power of the beam transmitted through the polarizer was measured as the half wave plate was rotated with a one degree increment. The one degree increment approximately corresponded to 10 nJ. Energies were calculated by dividing the power by the laser repetition rate and the curves were fitted to:

$$E(nJ) = E_0 cos^2 2(\theta - \theta_{shift}), \tag{2.1}$$

Since intensity, and hence energy, is proportional to the square of the electric field the square of the transmitted component was considered. Figure 2.3 shows a sample of the energy calibration curves used in our experiments.

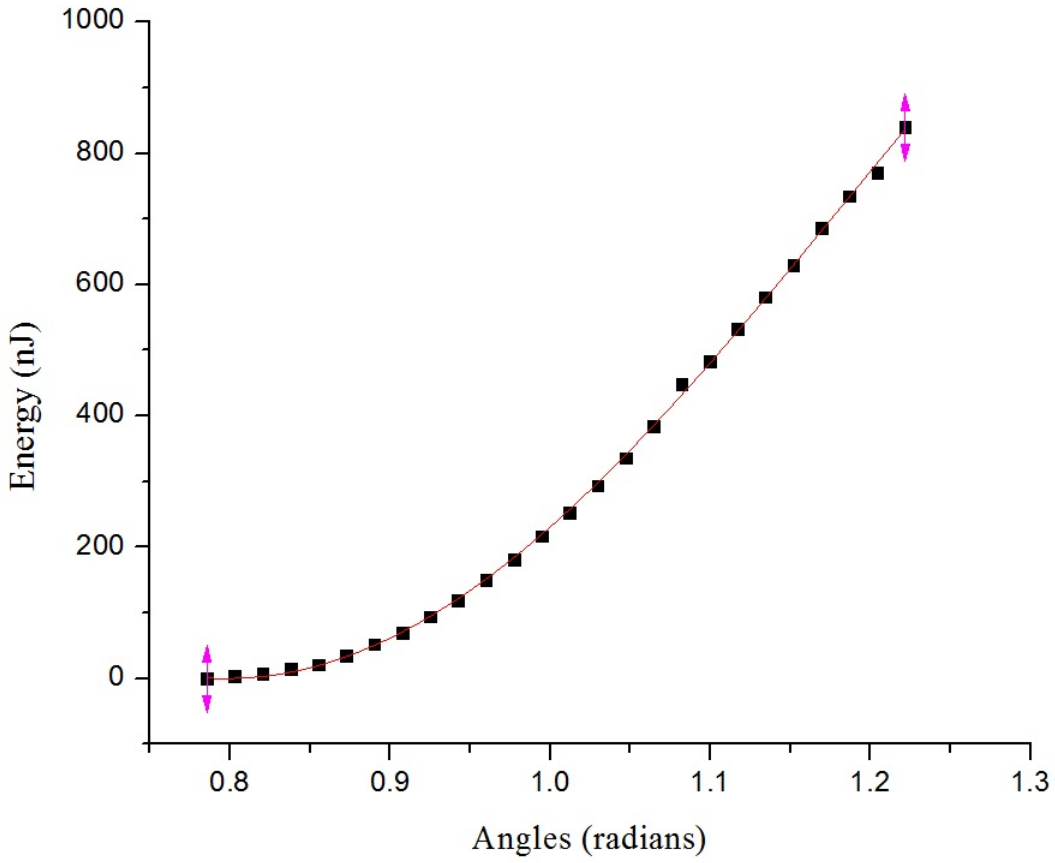


Figure 2.3: Energy calibration curve

## 2.2 Determining the laser spot size

Fluence is an important varied parameter in laser ablation experiments. It requires accurate knowledge of the radius of the beam at the focus $w_0$, also known as the spot size or the beam waist. At the focus, the spot size is defined to be the radius from the centre of the Gaussian to the point where the intensity has decreased to $1/e^2$ of the peak intensity. There are often slight differences between laser systems, which reflect in the energy of a pulse, thus quoting in terms of fluence nullifies the differences.

A titanium-sapphire laser system generates pulses that are spatially and temporally Gaussian. The Rayleigh range of a Gaussian beam is the length from the location of the beam waist to the location where the beam radius has increased by a factor of the square

root of two. The Rayleigh range is defined as:

$$z_0 = \frac{\pi w_0^2}{\lambda} \tag{2.2}$$

with $w_0$ and $\lambda$ being the beam waist and the wavelength of the light respectively. The definition of the range can be clearly understood from the following beam radius equation:

$$w(z) = w_0 \sqrt{1 + \left(\frac{z}{z_0}\right)^2}, \tag{2.3}$$

where the position z, along the direction of propagation, equals the Rayleigh range $z_0$, then the beam radius $w(z_0) = \sqrt{2} w_0$. Thus, the cross section of the beam along the propagation direction will be twice the area of the cross section at the beam waist.

The spot size was determined by using the knife-edge method. This method entails incrementally moving a knife-edge across the beam along one axis and measuring the output power. Then, by assuming a Gaussian laser intensity, appropriate fits were made to the data as will be discussed below. Another common method of determining the spot size is to ablate the surface at increasing energies and then plotting the diameter of the ablation as a function of energy. Then, the spot size is interpolated from the logarithmic relation of the diameter on fluence. The disadvantage of this method is that the spot size is interpolated whereas the knife-edge method allows for direct measurement.

The knife-edge method was used to measure the waist of the objective lens used in our experiments. The setup of the method is shown in Figure 2.4. The detector was placed

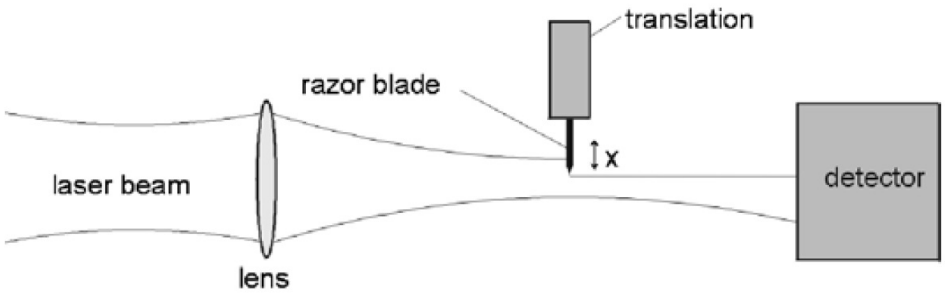


Figure 2.4: Knife-edge setup for spot size measurement [3].

after the knife-edge to measure the power of the unblocked beam by converting it to a voltage. Figure 2.4 shows a knife-edge cutting the beam along the x-axis at a particular z value that is within the Rayleigh range. In our experiment the data was collected by

placing the edge at a position of z below the focus and labelled by $-500$; this position was only estimated to be 500 microns below the focus. Five scans were performed at different approximate positions within the Rayleigh range; for z=$-750$, $-250$, 250, and 500. At this fixed z position the edge was moved along the x-direction in increments that varied between $100 - 0.25$ microns depending on the gradient of the measured voltage. The error bars in Figure 2.5 are the reading error of the oscilloscope. The x positions are also arbitrary and do not correspond to the exact locations across the beam. At the beginning of the scan the voltage is the highest because the full beam is measured, then as the edge is moved the reading slowly and then abruptly drops before it plateaus again when the beam is completely covered as demonstrated in Figure 2.5. The fitted line on the graph is [3]:

$$V(x) = \frac{V_{total}}{2}\left(1 + erf\left(-\sqrt{2}\frac{x - x_{shift}}{w_0}\right)\right) + V_{bg} \tag{2.4}$$

with the error function defined as:

$$erf(x) = \frac{2}{\sqrt{\pi}}\int_0^x e^{-u^2}du. \tag{2.5}$$

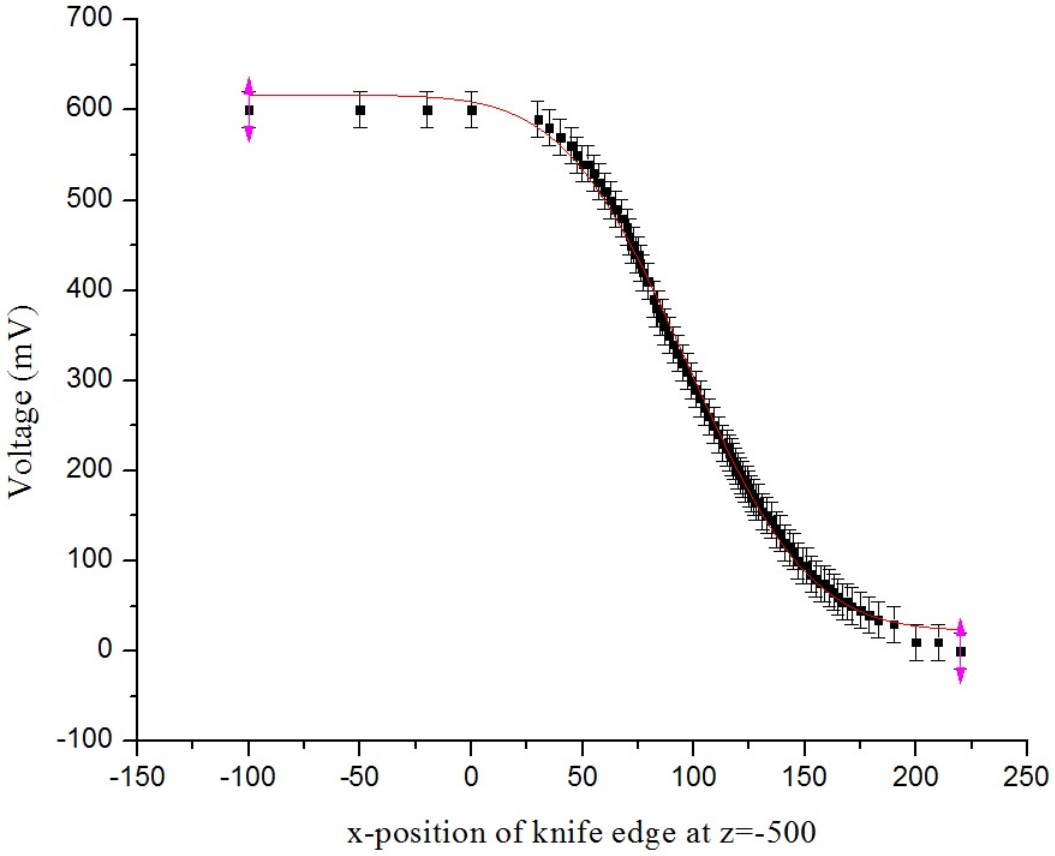


Figure 2.5: Knife-edge voltage scan across beam. The independent axis is in units of $\mu$m.

The beam waist parameters and their associated errors from the fits were plotted in Figure 2.6. In Figure 2.6 the beam radius equation was fitted to the plot with the ultimate beam waist as the sole parameter, since it is also contained within the Rayleigh range. For the 0.25 numerical aperture 16X magnification objective lens used in our experiments, the beam waist was determined to be $1.71 \pm 0.01 \mu m$ with the error being from the fitting. By considering the reading error of the oscilloscope and the propagation of errors, the true error is $\approx 0.3\mu$m and not the fitting error. The measured radius is close to the theoretical value of $1.95 \mu m$ by assuming that the radius of the spot is the radius of the first Airy disk [27]:

$$w_0 = \frac{1.22\lambda}{2NA}. \tag{2.6}$$

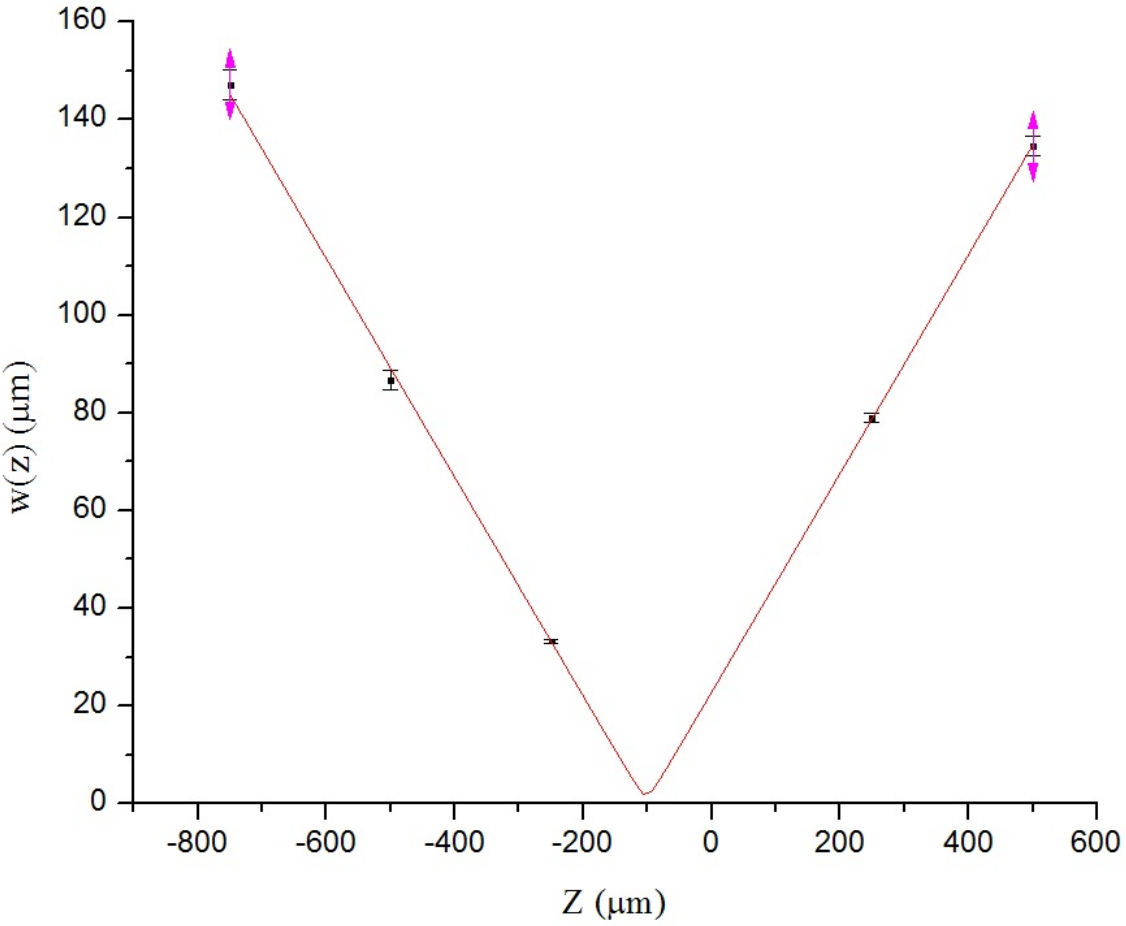


Figure 2.6: The points on the graph are the minimum radii measured at five different z-positions along the beam. The fitted curve is the beam waist equation 2.3.

$\lambda$ is the laser wavelength: 0.8 $\mu m$, NA is the numerical aperture: 0.25, and 1.22 is related to the root of the Bessel function used to calculate the intensity distribution of the diffracted beam.

## 2.3 Characterization of laser modified regions

Surface images were taken with the Jeol scanning electron microscope (SEM) using a 5 kV electron beam. To ensure electrical conductivity, and to minimize charging effects the silicon wafers were gold coated. The focused electron beam scanned the surface and

the images were collected by detecting the secondary electrons. This specific detector was used because secondary electrons are ejected from a thin layer with a thickness on the order of a nm. Since secondary electrons are emitted from a thin layer, they provide the best surface information in comparison to other ejected electrons. Three dimensional profile information primarily of the single pulse structures was collected using the Veeco atomic force microscope (AFM) in contact mode and a Bruker probe with a pyramidal tip radius of 10 nm, spring constant k=0.24 N/m, with front, back, and side angles of $15^0$, $25^0$, $17.5^0$, respectively. The AFM acquisition method will now be explained. A laser is incident on the probe and its reflection is detected by a set of photodiodes. As the probe scans the surface its height will change, thus the angle of the reflected light changes and it is detected at a different spot on the diodes. The difference in location of detection between reflections determines the height differences. TEM images and electron diffraction patterns were made by a FEI Tecnai G2 transmission electron microscope. TEM images can have a spatial resolution of 0.144nm. Electrons will propagate through the sample and are detected; the brighter the images the greater the number of unscattered transmitted electrons. In order to use the TEM the sample must be transparent to electrons. Therefore, a slice of the sample with thickness less than the attenuation length of the electron beam needed to be made. Fibics company made the slice using a $Ga^{2+}$ focused ion beam. They first coated the sample with carbon and then with titanium to protect the surface from the beam. Photoluminescence (PL) spectra were collected for N-type silicon. PL is the process of exciting a surface by laser irradiation at wavelengths that excite different electronic states. Then, the emission of the excited sample is collected and the variation in the peaks and intensities of the emitted light give information about the sample.

# Chapter 3

# Single pulse microstructuring of silicon

Insight into the fundamental processes that govern laser ablation as a function of laser parameters such as pulse energy and polarization can be obtained by investigating interactions of a single laser pulse with the material. Silicon was the material of choice because of its wide range of applications in photonics. Femtosecond laser pulses were used to structure the surface of N-type, P-type, and intrinsic silicon to study how the electron density variations influence the dynamics of microstructuring. We investigated the evolution of the structures by varying the pulse energy (sections 3.1 to 3.3) and the laser polarization (section 3.4). All silicon samples had a thickness of approximately 400 $\mu$m and have (100) orientation.

## 3.1 N-type

N-type silicon is doped with phosphorous with estimated electron density of $10^{16} cm^{-3}$ at room temperature. Figure 3.1 shows a set of scanning electron microscope images taken for the average energy range of 45 - 130 nJ for N-type. The dimensions of the ring and the crater appear to increase with increasing energy. The ring contrast in the SEM images is increasing with energy indicating that the height of the ring is also increasing.

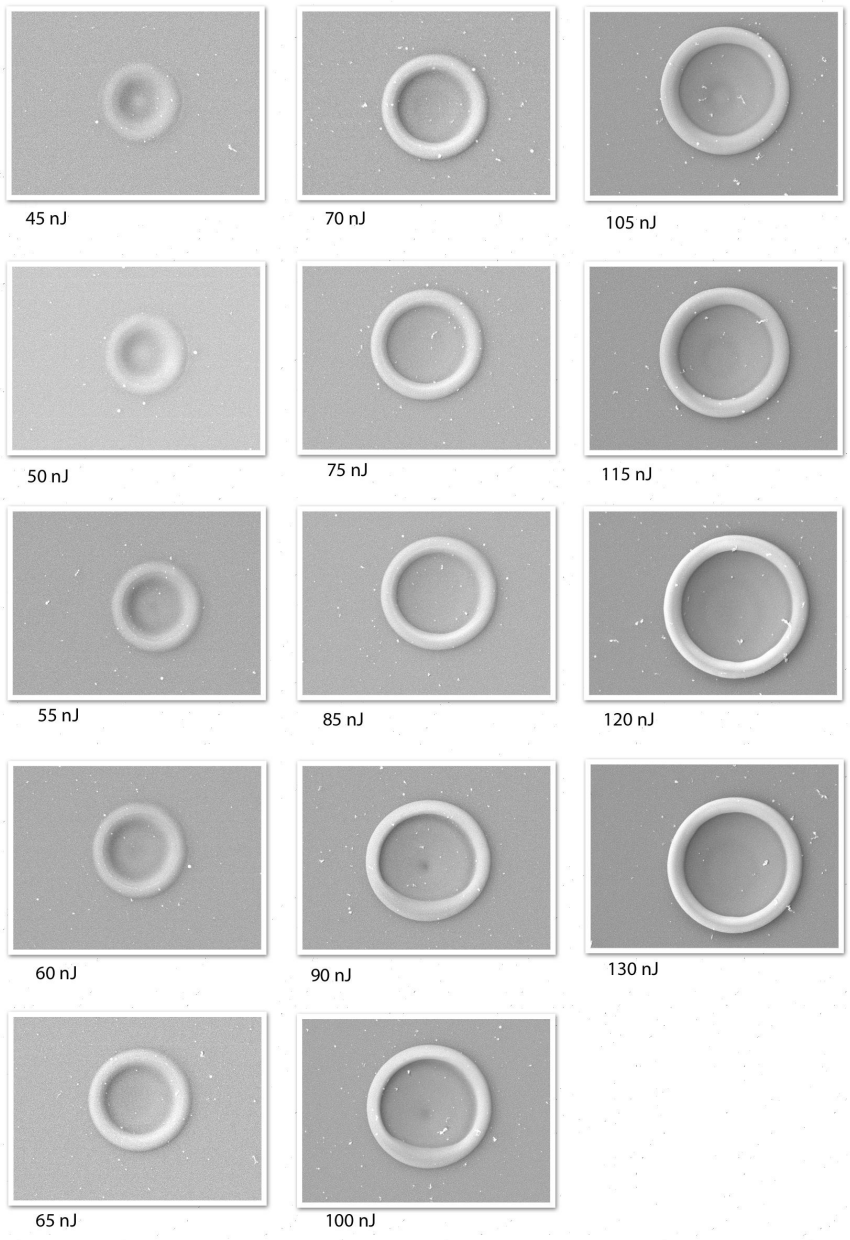


Figure 3.1: Set of N-type SEM images of silicon ablation craters generated by 40 fs pulses with pulse energies 45 - 130 nJ. The polarization is ↕.

It is clear that the diameter of the ring-like structure formed increases with energy.

Figure 3.2 shows that the dependence of the diameter on energy follows the logarithmic equation:

$$D^2 = 2w_0^2 ln\frac{\phi}{\phi_0} \tag{3.1}$$

where $w_0$ is the beam waist and $\phi_0$ is the damage threshold, as has been observed by many authors [3]. The damage threshold in our experiments was approximately 0.4 $J/cm^2$ and the literature value is about 0.3 $J/cm^2$ [2]. The literature value is within the 30% error in fluence caused by the knife-edge method. The error bars in Figure 3.2 are

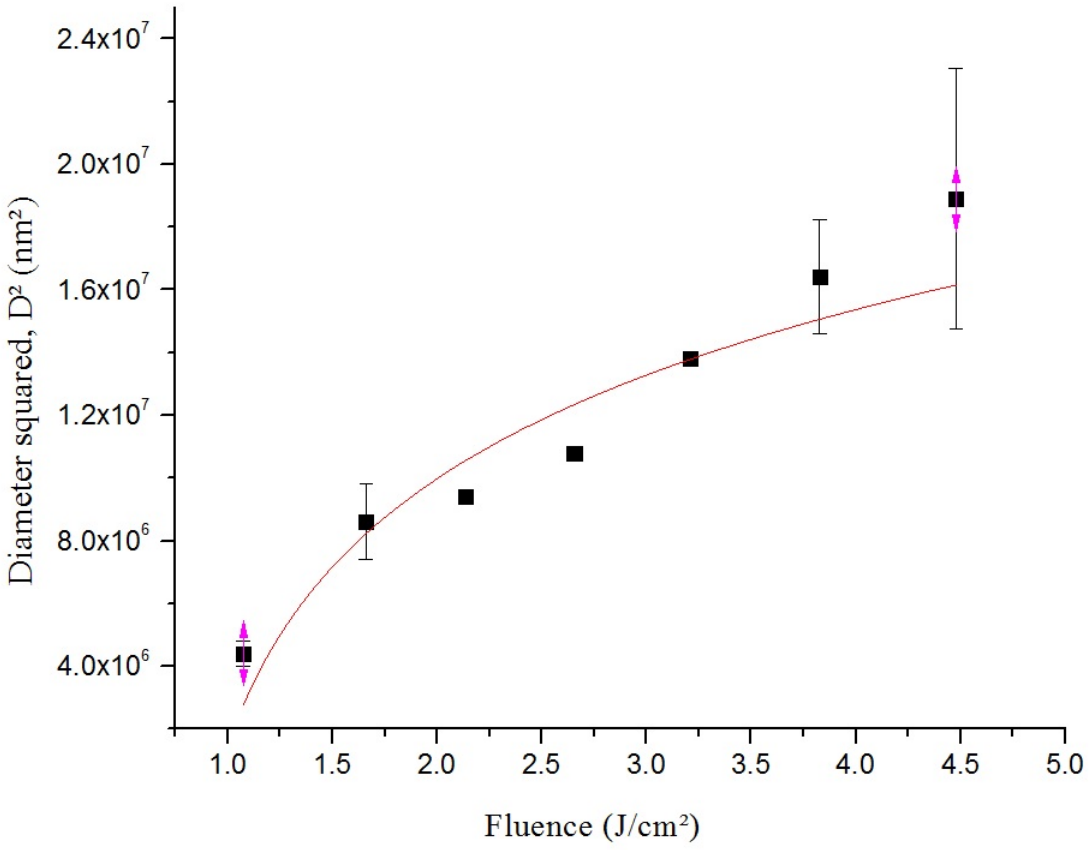


Figure 3.2: Outer diameter of the single pulse rings as a function of fluence is shown. The curve is equation 3.1; the beam waist and the threshold fluence are the fitting parameters.

the standard errors for two sets of rings. The standard error is calculated through the propagation of errors formula. For example a two variable function X has standard error

equal to:

$$\delta X = \sqrt{\left(\frac{\partial X}{\partial x_1}\right)^2 (\delta x_1)^2 + \left(\frac{\partial X}{\partial x_2}\right)^2 (\delta x_2)^2}. \tag{3.2}$$

For the data of Figure 3.2, the standard error of the diameter is $\delta D = \sqrt{((D_1 - D)^2 + (D_2 - D)^2)/2}$, and D is the average diameter of two rings. Thus after simplification the standard error for the square of the diameter shown in Figure 3.2 is:

$$\delta D^2 = 2D\sqrt{(D_1 - D)^2 + (D_2 - D)^2} \tag{3.3}$$

AFM analysis of the ring structures shown above provides detailed information on the dependence of the ring width, diameter, and height on pulse energy. The purpose of the following plots is to observe the effect that polarization has on the structures. The top panel of Figure 3.3 shows that the widths in the two orthogonal directions are increasing with fluence. However the widths along the polarization remain greater than the orthogonal direction for the entire fluence range used. The width asymmetry, defined as the ratio of the dimensions along and orthogonal to the polarization, is shown in the bottom panel. The width asymmetry fluctuates around 1.3 but doesn't appear to be increasing with fluence. The greater asymmetry ratio of the width implies that the cross section of the crater is becoming less circular with fluence. Whereas the overall modified regions remains circular.

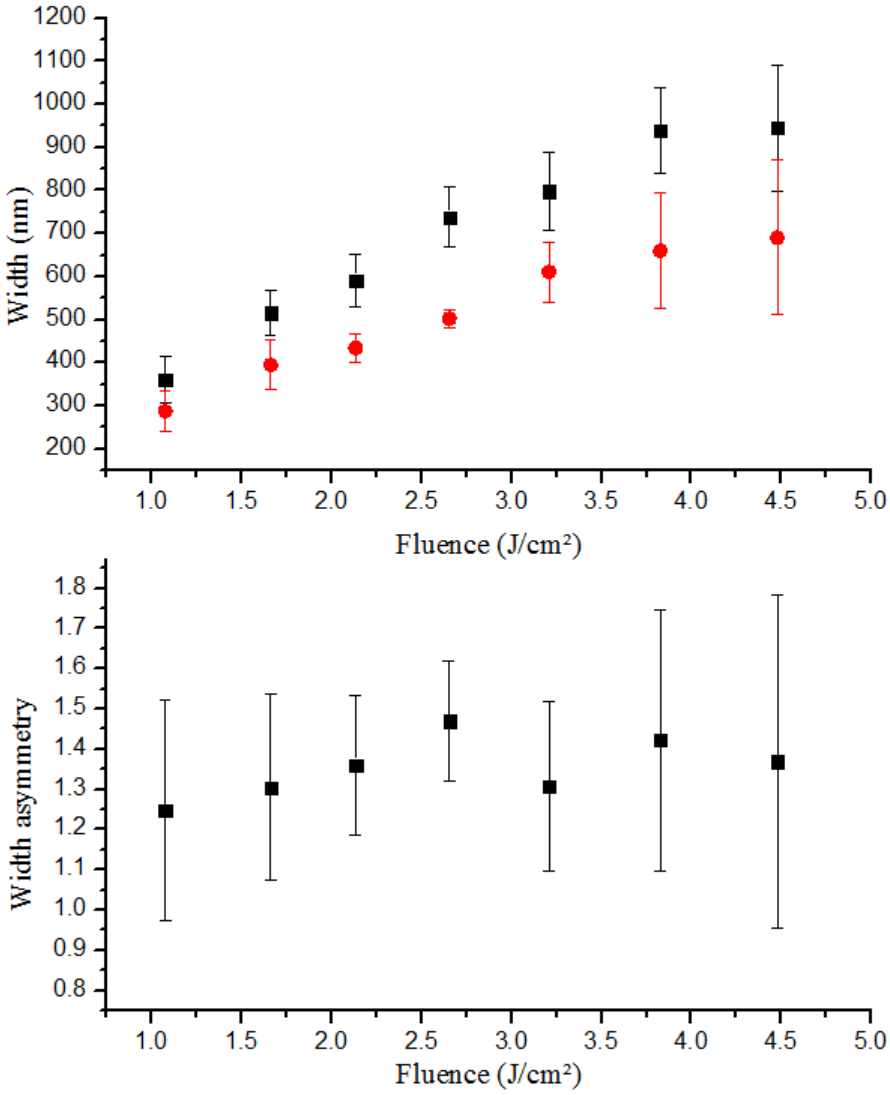


Figure 3.3: Widths and asymmetries for N-type silicon are shown. Black data points are dimensions along the polarization and red are dimensions perpendicular to the polarization.

Figure 3.4 shows the diameters of the ring structure along the two orthogonal directions and the diameter asymmetry. The asymmetry is not substantial; it fluctuates around 1.1 and 1.0 is within the error bars of the points, indicating that the ring structures are nearly circular. The following is an explanation of the measurement method

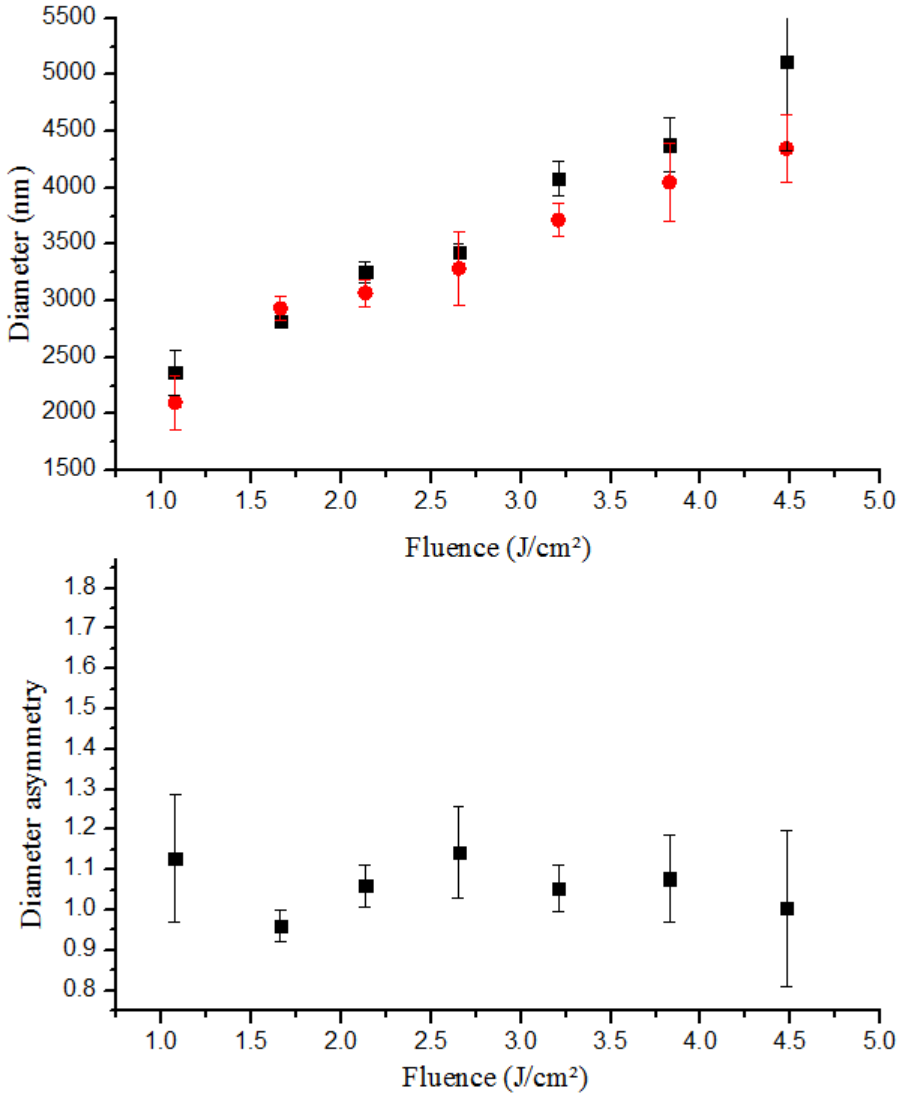


Figure 3.4: Diameters and asymmetries for N-type silicon are shown. Black data points are dimensions along the polarization and red are dimensions perpendicular to the polarization.

used for the ring widths and diameters. Starting at the edge of the AFM image and moving along or perpendicular to the polarization, the beginning of the ring is considered to be the pixel with a height that is 14 nm above the background. This threshold height needed to be established because the information given by the AFM scan does not set

the background to zero. Also, the plane of the background is not perfectly smooth so even subtracting the background does not suffice. The threshold height of 14 nm was chosen somewhat arbitrarily within a window of reasonable heights: 10 - 20 nm. The rationale is based on the fact that this window is less than ten times smaller than the width dimensions; hence, little information is lost. Asymmetry calculations are not affected by this measurement method since the ratios are calculated. The error bars of the widths and diameters are calculated with the error formula for the average of multiple measurements, similar to the error formula used in Figure 3.2. For the asymmetries, the error using the propagation of errors method is:

$$\delta w_{asym} = w_{asym}\sqrt{\left(\frac{\delta w_1}{w_1}\right)^2 + \left(\frac{\delta w_2}{w_2}\right)^2}, \tag{3.4}$$

$w_{asym}$ is the width asymmetry, and $w_1$ and $w_2$ are the widths of the rings parallel and perpendicular to the polarization. The same formula is applicable to the diameter and height asymmetries.

The atomic force microscope image in Figure 3.5 shows the three dimensional structure of the single pulses and it is clear that there is an asymmetry in the height of the rim. The axis containing the taller height is parallel to the polarization. Figure 3.6 shows the height and asymmetries. The asymmetry is calculated by taking the ratio of the height along and orthogonal to the polarization.

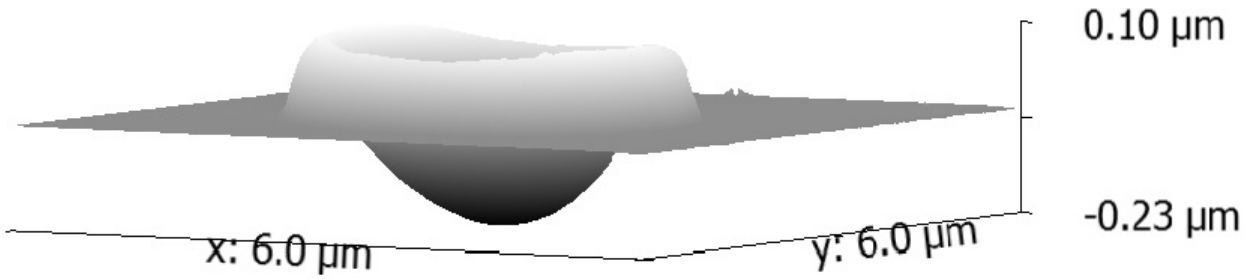


Figure 3.5: AFM image of N-type crater

The height asymmetry begins around 1.0, increasing to a maximum of about 1.35 around $2.75 J/cm^2$ and then decreases back to 1.0. This asymmetry trend is dissimilar to the width and diameter asymmetries.

Asymmetries in the width and height of the rim surrounding the crater are a consequence of the orientation of the polarization. This will be further discussed at the end of this chapter. In the literature similar asymmetrical behaviour has been observed in dielectrics. For instance, femtosecond laser ablation of PMMA resulted in elongation of the crater parallel to the polarization, when plasma density was overcritical, and perpendicular, when it was under critical [26]. For silicon, elongation of the crater is minimal and instead enhancement of ring height, and correspondingly of ring width, are the significant polarization effects.

### 3.1.1 Physics of the single pulse structure

The single pulse ring like structure is explained by considering the formation of the plasma and the process of transferring the absorbed laser energy to the lattice. The high intensity laser pulse ionizes the material at the beginning of the pulse and creates a plasma within the skin depth. Since silicon is a small band-gap material absorption is primarily linear which limits the interaction to within the skin depth. This is not the case for wide band-gap materials which absorb light nonlinearly causing the light to

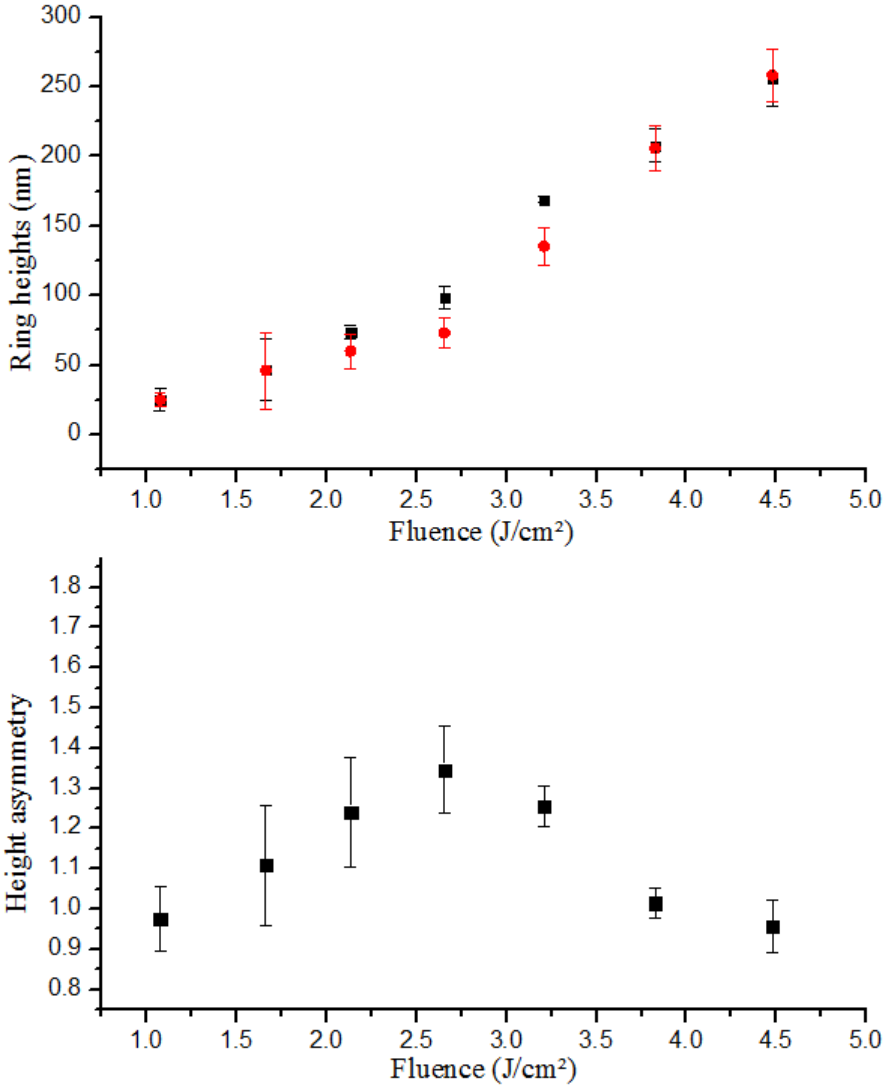


Figure 3.6: Height asymmetry for N-type silicon as a function of fluence is displayed. Black points correspond to heights parallel to the polarization and red correspond to the perpendicular heights.

penetrate more deeply and be limited by the Rayleigh range.

Plasma electrons continue to gain energy for the remainder of the pulse via inverse Bremsstrahlung. Equilibrium within the plasma is achieved near the beginning of the pulse, thus for the remainder of the pulse the energy distribution follows the Gaussian

profile of the intensity. The spatial intensity distribution is transferred to the plasma resulting in a spatial gradient in electron density within the plasma that decreases radially from the centre. Electron relaxation transfers energy to the lattice causing it to melt and increasing the hydrodynamic pressure. A shockwave within the material is generated approximately 1ps [28] after the pulse when the lattice has been heated. It occurs on the nanosecond timescale since the velocity of sound in silicon is nearly $10^4 m/s$ and the diameter of the structure is on the order of microns. The distribution of laser energy absorbed by the particles follows a Gaussian function due to the Gaussian intensity profile of the laser. Therefore, the shockwave or the profile of the magnitudes of the particle velocities also follows a Gaussian profile. The centre of the irradiated region was exposed to the most intense part of the pulse so the particles at the centre possess the greatest velocities and thus travel the greatest distance. Accordingly, the particles at the outskirts of the irradiated region travel the least. The shockwave moves the particles away from the centre with a deceleration as they approach the cold boundary of the non-irradiated surrounding. Particles begin to pile up at the cold boundary and create a rim around the resulting crater.

The plasma density gradient depends on how much higher or lower the peak fluence is than the threshold fluence of ionization. For instance, a pulse with peak fluence greater than the threshold will produce a plasma with a constant density in the central portion where the fluence is greater than the threshold. The density will gradually decrease radially away from the centre. Sharpness of the gradient is reflected in the shape of the crater formed. For lower fluences around 0.6 $J/cm^2$ the crater is V-shaped and at higher fluences around 2 $J/cm^2$ the crater is U-shaped [29]. Although the authors of [29] performed their experiments with over 100 pulses our results show similar changes in the crater formation in the same fluence ranges. Figures 3.7 and 3.8 show the craters formed around the same fluences.

At low fluences the gradient follows the intensity profile which means that the central portion of the irradiated spot will have more material pushed out than the adjacent sides due to the higher kinetic energy of the particles. On the other hand, at higher fluences the spatial gradient is flatter in the central region and falls off less sharply adjacently resulting in smoother motion of particles.

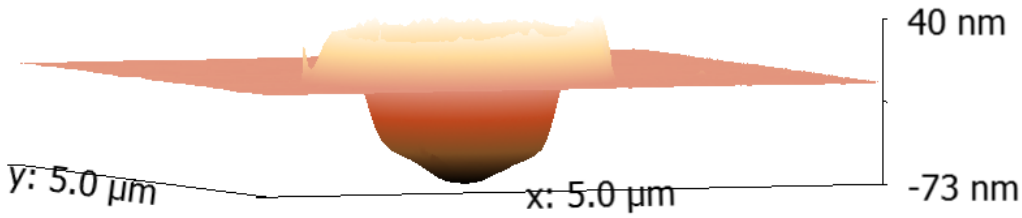


Figure 3.7: AFM image of the structure created by a 0.6 $J/cm^2$ pulse on N-type silicon. The V-shape of the crater is observed.

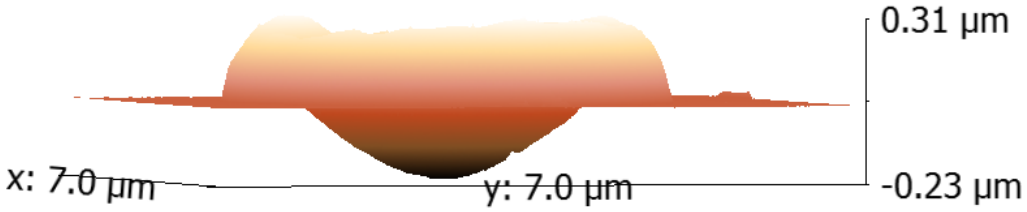


Figure 3.8: AFM image of the structure created by a 2 $J/cm^2$ pulse. The crater shape is much smoother than in Figure 3.7, resembling the letter U.

## 3.2 P-type

For P-type the enhancement of height and consequently of the ring width was orthogonal to the polarization. Figure 3.9 displays the widths and their asymmetries, and Figure 3.10 shows the diameters and their asymmetries as functions of fluence. The evolution of the orthogonal diameters is very similar to the N-type, however there are differences between the evolutions of the widths for the two types. For instance, in Figure 3.9 the asymmetry of the width appears to be decreasing at a faster rate than the rate of increase the N-type (Figure 3.3).

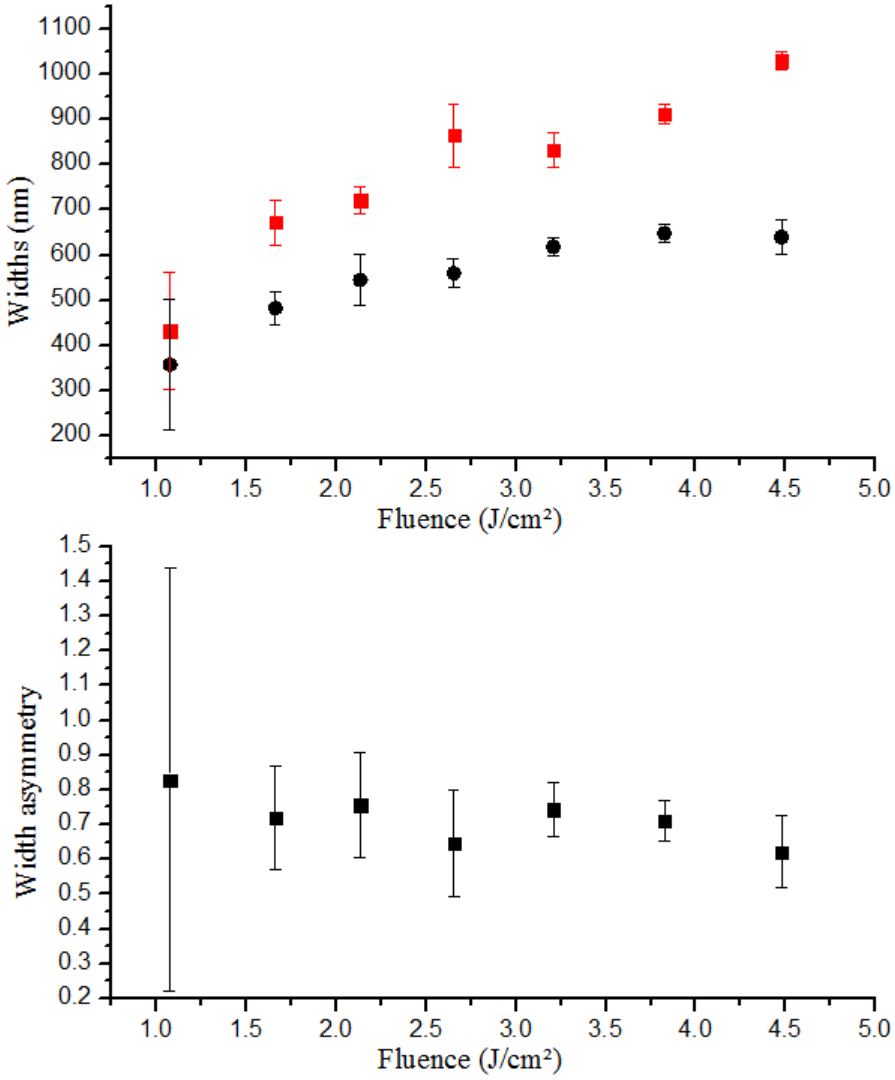


Figure 3.9: Widths and asymmetries for P-type silicon are shown. Black data points are dimensions along the polarization and red are dimensions perpendicular to the polarization.

Figure 3.11 shows that the height asymmetries begin around 1, then decrease and remain below 1. Only the first ring contains 1 within uncertainty. After the decrease the asymmetry fluctuates around 0.85. The trend does not contradict the explanation for the N-type trend. Plasma density remains much lower than the critical density hence the index of refraction is real and positive and thus propagates through the plasma. Within

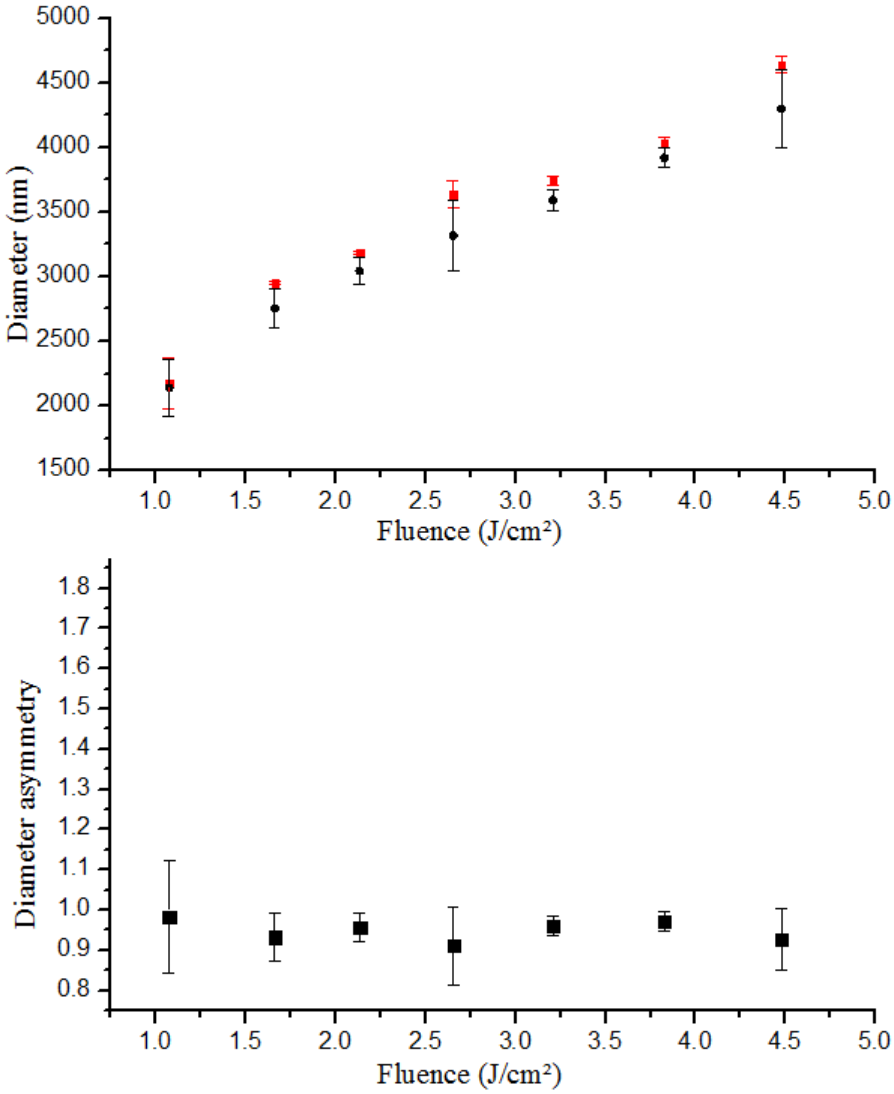


Figure 3.10: Diameters and asymmetries for P-type silicon are shown. Black data points are dimensions along the polarization and red are dimensions perpendicular to the polarization.

the plasma the field will become enhanced perpendicular to the incident field. These field enhancements are different for P-type and N-type because the dielectric functions are different due to their different plasma densities. This will be further discussed later in the chapter.

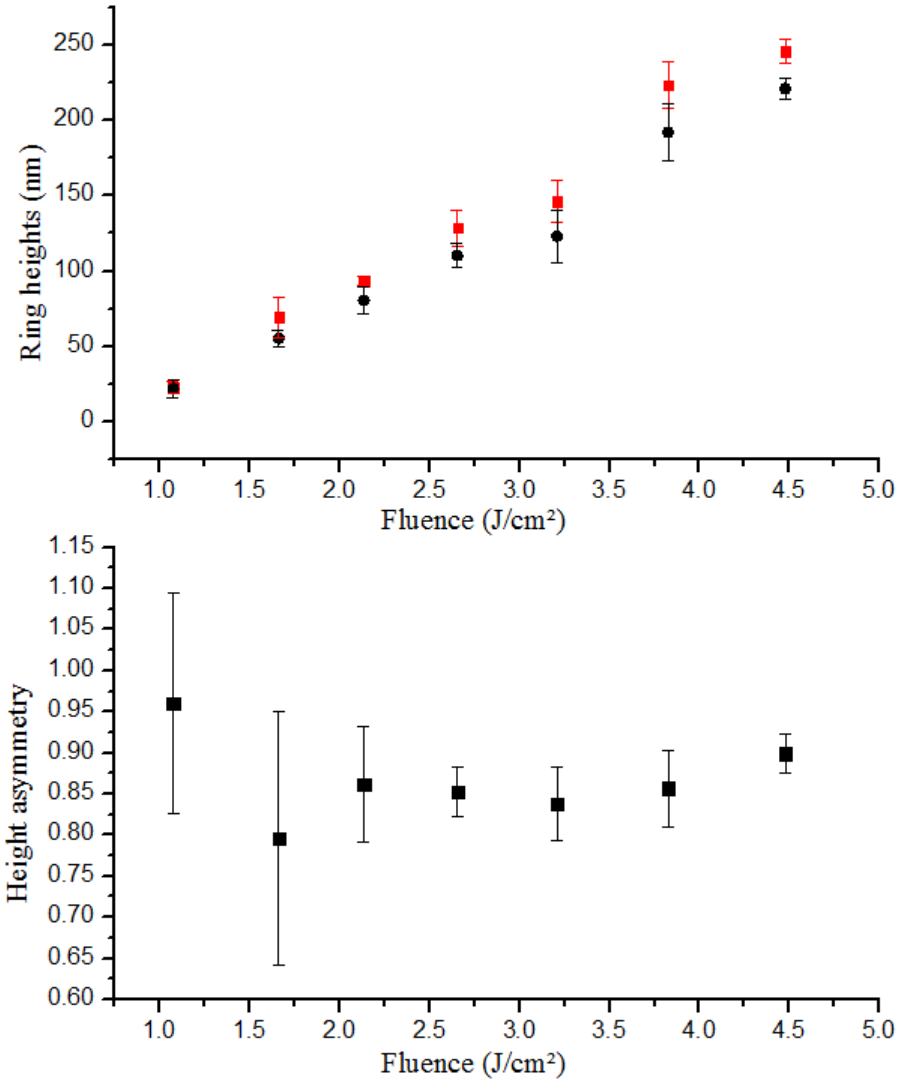


Figure 3.11: Height asymmetry for P-type silicon as a function of fluence is displayed. Black points correspond to heights parallel to the polarization and red correspond to the perpendicular heights.

## 3.3 Intrinsic

Figure 3.12 shows the width and its asymmetry, and Figure 3.13 shows diameter and its asymmetry as functions of fluence for intrinsic silicon. Identical to N-type and P-type, the asymmetries were determined by measuring the dimension parallel to and dividing it

by the dimension orthogonal to the polarization. The width asymmetry plots for N-type and intrinsic both appear to be fluctuating around 1.4, whereas for P-type the ratio decreases with fluence (Figure 3.9). As the fluence increases plasma density increases and it is expected that the behaviour of intrinsic silicon will more resemble N-type than P-type.

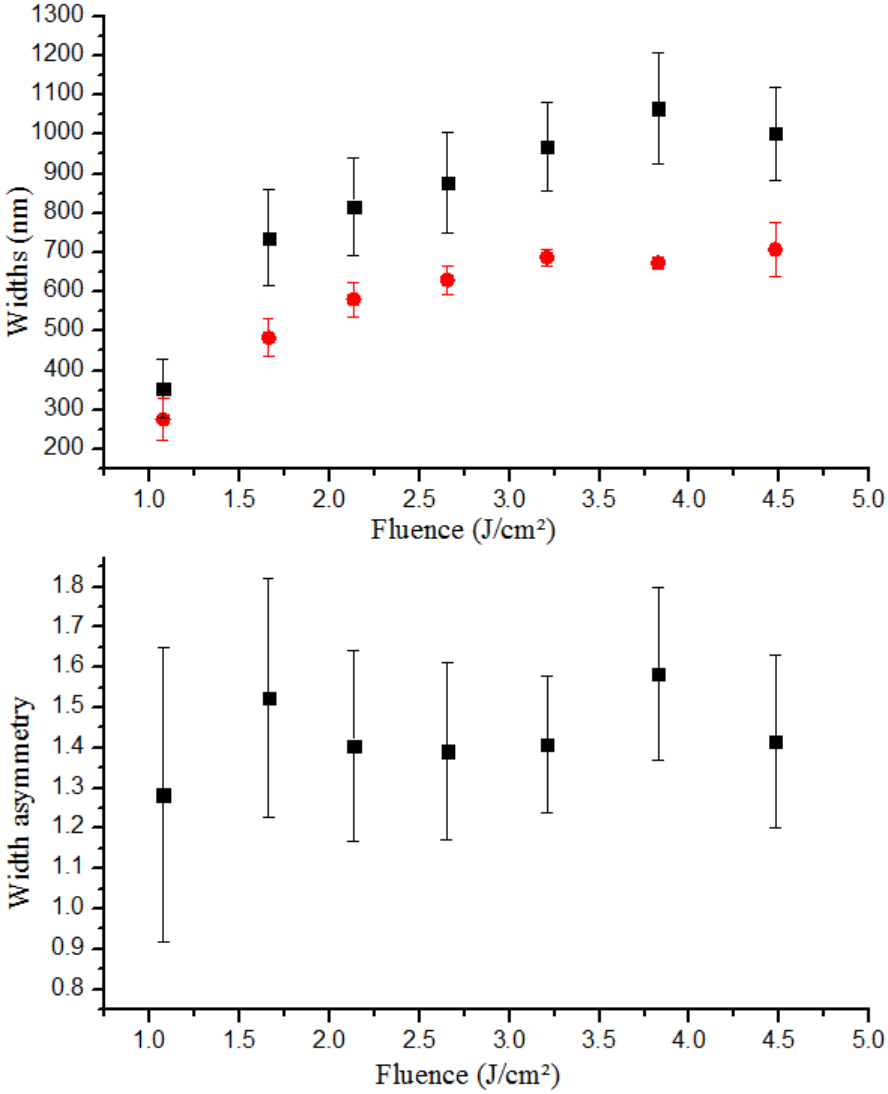


Figure 3.12: Widths and asymmetries for intrinsic silicon are shown. Black data points are dimensions along the polarization and red are dimensions perpendicular to the polarization.

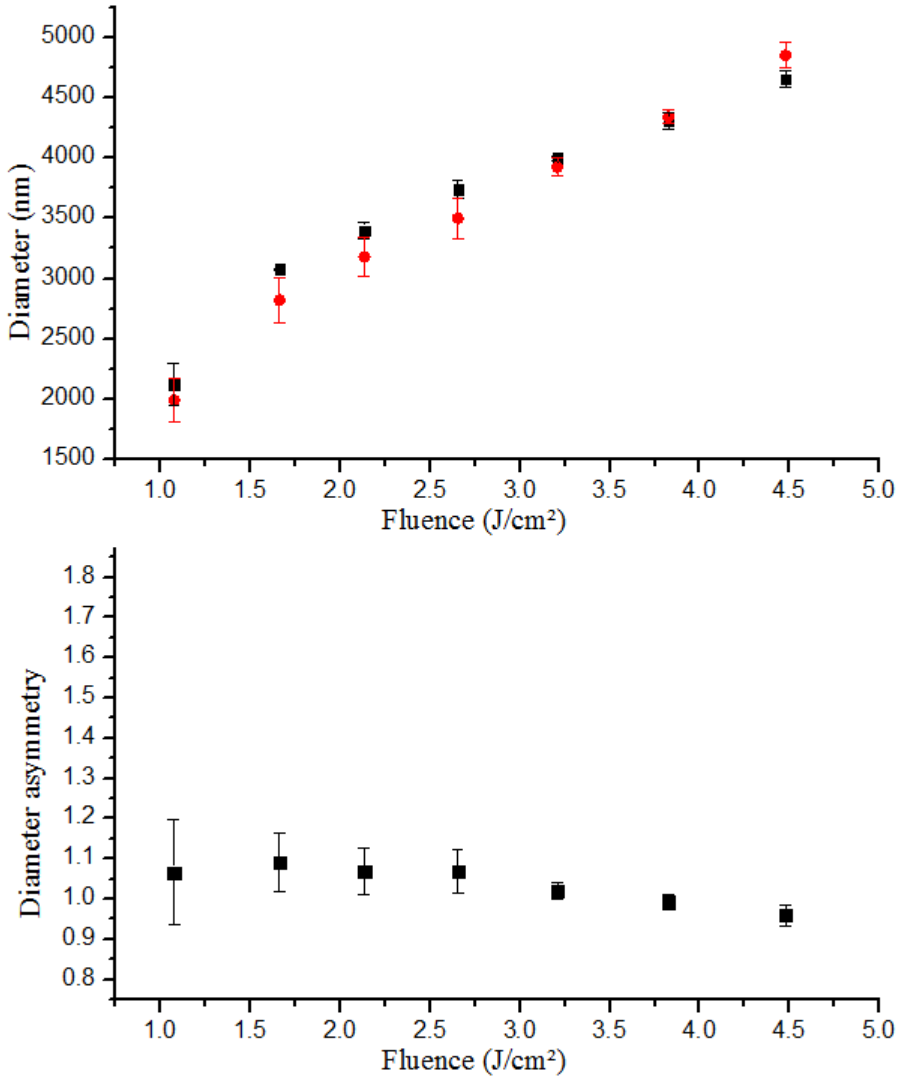


Figure 3.13: Widths and asymmetries for intrinsic silicon are shown. Black data points are dimensions along the polarization and red are dimensions perpendicular to the polarization.

Figure 3.14 shows how the ring heights and their asymmetry vary with fluence. Similar to N-type, the height asymmetry steadily increases until a certain fluence, and then abruptly decreases. The primary difference is that the fluence corresponding to the maximum asymmetry is greater for intrinsic. According to the N-type theory the peak occurs when the density is overcritical. Due to the fact that the conduction electron density for

intrinsic is much less than for N-type, the fluence required to make the plasma overcritical should be necessarily greater.

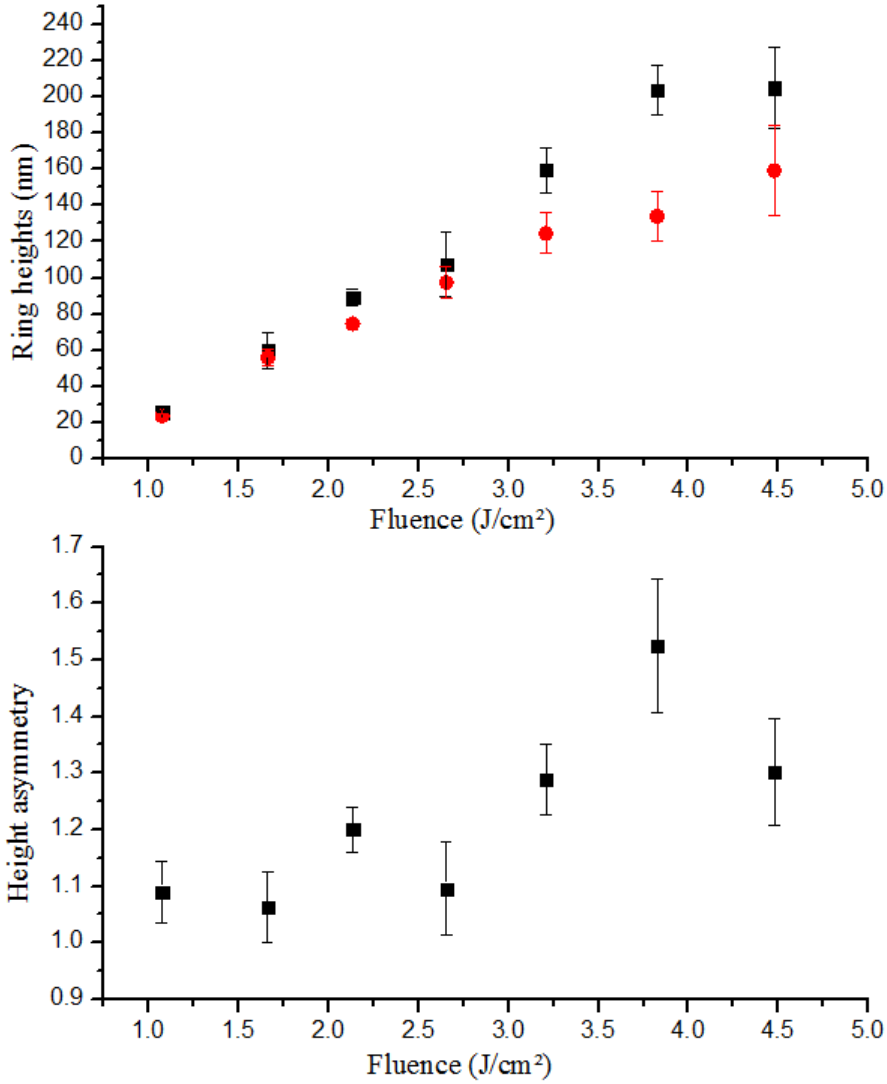


Figure 3.14: Height asymmetry for intrinsic silicon as a function of fluence is displayed. Black points correspond to heights parallel to the polarization and red correspond to the perpendicular heights.

## 3.4 Polarization dependence

There are asymmetries in the width and height of the rim surrounding the crater that are a consequence of the orientation of the polarization, which are demonstrated in Figures 3.3, 3.6, 3.9, 3.11, 3.12, and 3.14. It was observed in these figures that, along the direction of the electric field, dimensions were greater than perpendicular to it for N-type and intrinsic silicon. The opposite effect was observed for P-type. This section presents data and a discussion on the polarization dependence of the single pulse structure. This discussion can also be further linked to the multiple-pulse structures presented in the next chapter.

Figure 3.15 are colour maps of the N-type single pulse structures acquired using an AFM. They were produced by $1.7 J/cm^2$ pulses using a quarter and a half wave-plate. The lines show the axes along which the height asymmetries have been calculated. For the linearly polarized structures the bold line shows the axis of the electric field. The height asymmetry in linearly polarized structures is depicted in the line profiles of Figure 3.15. The black curve is the profile parallel to the field and the red is perpendicular. It is clearly observed that the black curve sits higher than the red. It is believed that the motion of material favours the direction of polarization. Thus, it is expected that the height asymmetry would disappear for circularly polarized light since the field oscillates along the polar radius with angle $2\pi$. For the two linearly polarized structures the asymmetries are calculated by dividing the average of the heights along the bold line by the average of the heights along the faint line.

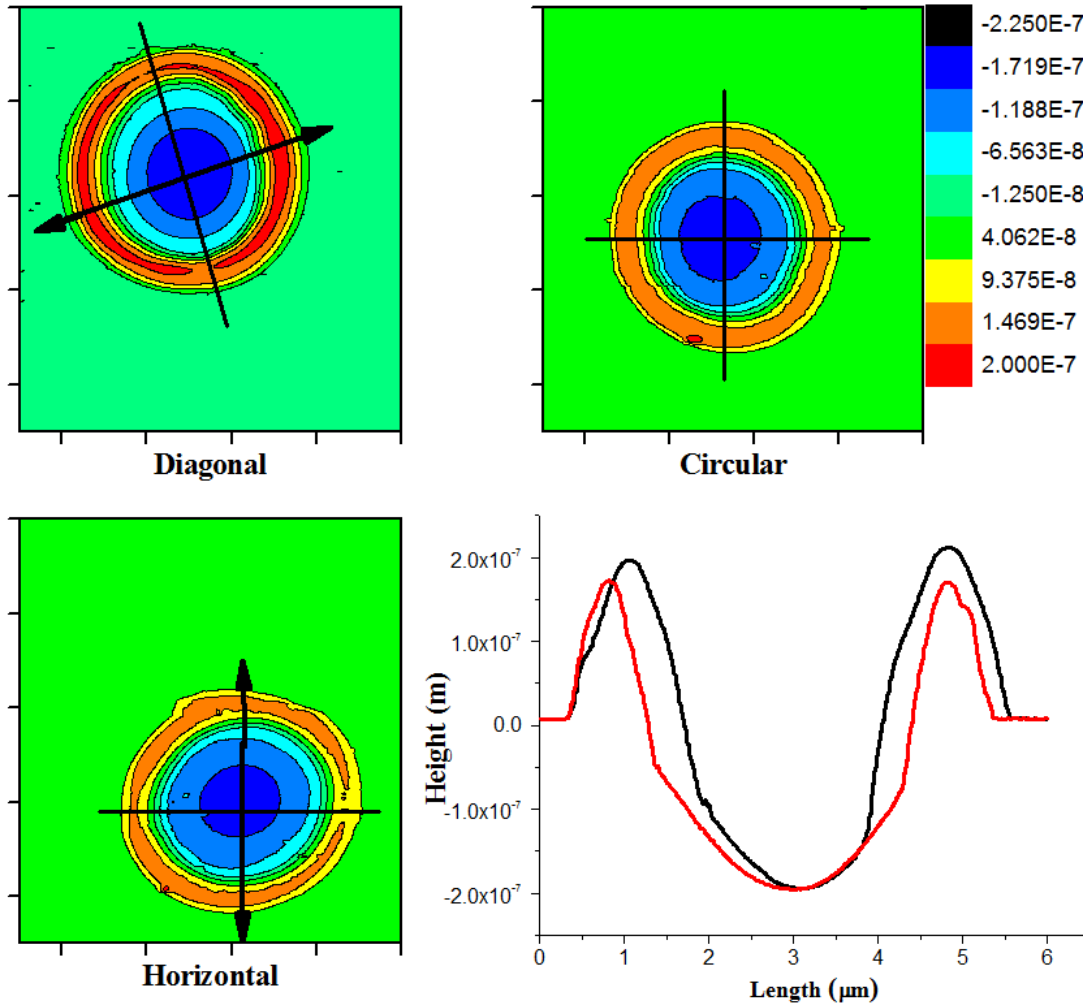


Figure 3.15: Single pulse irradiations with three different polarizations on N-type silicon. The lines on each map correspond to the axes where the height asymmetries were calculated. The bold lines show the direction of the electric field. The polarizations are written below the images and the values of the asymmetries are written on the left hand sides. In lower right hand corner, line profiles of the linearly polarized structure are shown: black is parallel and red is perpendicular to the field.

Preferential absorption of p-polarized light at oblique incidence, resonance absorption, has been known for a long time [30]. Tight focusing of light by the objective lens meant that a cone of photons was focused onto the surface, thus many were obliquely incident even though the beam was normal. Preferential absorption of p-polarized light may be able to explain enhancement of heights and widths for N-type and intrinsic

silicon. However, since resonance absorption predicts that there will be an enhancement of absorption parallel to the electric field then this mechanism cannot be responsible for the enhancement observed on P-type silicon.

Instead of resonance absorption, asymmetries can be linked to field enhancement caused by under and overcritical plasma densities. As explained in the introductory chapter, electrons are excited to the conduction band and achieve equilibrium within $10^{-2}$ fs. When equilibrium is established, they collectively oscillate and their motion is assumed to be that of an electron on a spring. Then, the oscillating electrons interact with the incident radiation in a manner that depends on the plasma density. When the plasma is overcritical there is enhancement in the height and width of the ring parallel to the electric field which is the case for N-type and intrinsic silicon. Enhancement is perpendicular to the electric field when the plasma is under dense, which is the case for P-type silicon.

A possible explanation for the decreasing height asymmetry observed in Figures 3.6 and 3.14 is that the plasma density has become overcritical making the index of refraction real and negative, thus reflecting most of the incident light. Therefore, there will no longer be an influence of the polarization to the formation of the plasma and ultimately of the ring; height asymmetry disappears.

In [4] the asymmetrical effects are explained by considering the plasma as a spheroid, calculating the electric field at the poles and the equator based on geometry, and determining the field enhancement by calculating the ratio of the fields at the pole and the equator. Figure 3.16 shows the spheroid and the fields at the pole and the equator. The under and overcritical plasma density cases are shown with the resulting enhancements. In Figure 3.16 E is the magnitude of the applied electric field and $\epsilon$ is the permittivity of the plasma defined as the quotient of the real part of the dielectric function of the plasma and the dielectric constant of the surrounding medium: $\epsilon = \frac{\epsilon_r}{\epsilon_d}$. Metals have a high density of conduction electrons and hence the authors in [4] used a metal spheroid to model the overdense case even though the material was a dielectric. A metal has all of its conduction electrons on the surface where they arrange themselves to make the electric field zero within the volume. When an external electric field is applied like a laser beam the charges oscillate parallel to the field and emit radiation primarily perpendicular to their direction of oscillation. According to the electric field boundary conditions defined by Maxwells equations: the electric field parallel to the metal interface is continuous and is discontinuous perpendicular to it. Due to the facts that the electric field within a metal must vanish and fields parallel to the interface must be equal then only the field

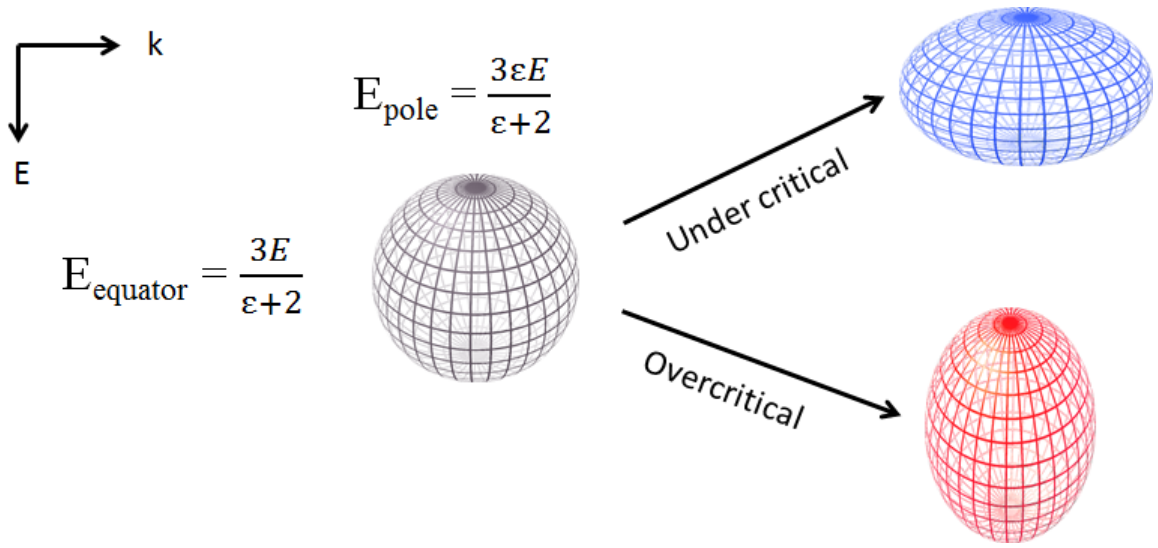


Figure 3.16: Field enhancement and the field equations for a spheroid. The two cases of under and overcritical plasma densities are shown with their resulting enhancements. E is the direction of the incident electric field and k is propagation vector.

perpendicular to the interface survives. Therefore, constructive interference between the radiation emitted by dipoles and the incident light resulting in field enhancement is possible only at the poles of the spheroid with the axis parallel to the polarization. Metal spheroids are no longer an appropriate analogy when the underdense case is considered, because the density of conduction electrons is very low; instead a dielectric spheroid is employed.

By controlling the fluence to change the plasma density from under to overcritical, the properties and hence response of the material also change. The response of a material to an applied electric field can be quantified by the permittivity. For a dielectric the permittivity is positive and less than one whereas for a metal it is negative with an absolute value greater than one. By calculating the resultant fields produced by interference of the emitted dipole radiation and the incident field, it is clear that for dielectrics the field at the equator dominates and for metals the fields at the poles dominate. The response time of each material to the laser is considerably different due to the difference in their permittivities. Due to the high magnitude of the permittivity of a metal, the oscillating dipoles emit radiation immediately when in the presence of the external field, and thus, the fields constructively interfere resulting in field enhancement. However, for a dielectric the dipoles are not as quick to respond and therefore require time before they oscillate

at the laser frequency, thus their emitted radiation is predominantly out of phase with the laser. Since the emitted dipole radiation is out of phase with the incident field, the fields at the poles are nearly cancelled and along the equator the field is comparatively substantial. For intrinsic and N-type the plasma frequency initially is not greater than the critical frequency, only during the pulse do they exceed it. In order to calculate the plasma density to know if it becomes overcritical, the following system of differential equations needs to be solved [13]:

$$\rho C_L \frac{\partial T(x,t)}{\partial t} = \frac{\partial}{\partial x}\left[\kappa_L \frac{\partial T(x,t)}{\partial x}\right] + \frac{3k_B n(x,t)\rho C_L}{3k_B n(x,t) + \rho C_L}\frac{T_C(x,t) - T(x,t)}{\tau_E} \tag{3.5}$$

$$\frac{\partial n(x,t)}{\partial t} = \frac{\partial}{\partial x}\left[D_\alpha \frac{\partial n(x,t)}{\partial x}\right] + \alpha_L \frac{I(x,t)}{hf} + \beta \frac{I(x,t)^2}{2hf} - \frac{n(x,t)}{\tau_R} \tag{3.6}$$

$$\begin{aligned}\frac{\partial U_C(x,t)}{\partial t} = {} & \frac{\partial}{\partial x}\left[\frac{U_C(x,t)}{n(x,t)} D_\alpha \frac{\partial n(x,t)}{\partial x}\right] \\ & + \left(\frac{hf - E_g}{hf}\alpha_L + \frac{2hf - E_g}{2hf}\beta I(x,t) + \alpha_{FCA}\right) I(x,t) \\ & + E_g \frac{n(x,t)}{\tau_R} - \frac{3k_B n(x,t)\rho C_L}{3k_B n(x,t) + \rho C_L}\frac{T_C(x,t) - T(x,t)}{\tau_E}\end{aligned} \tag{3.7}$$

$$\frac{\partial I(x,t)}{\partial x} = -\left(\alpha_L + \beta I(x,t) + \alpha_{FCA}\right) I(x,t) \tag{3.8}$$

The carrier energy is related to the temperature through:

$$U_C(x,t) = 3k_B n(x,t) T_C(x,t) \tag{3.9}$$

The system of equations is based on the two-temperature model, which shows how the system reaches equilibrium by individually considering the evolutions of the electron and lattice temperatures [31]. The system is one dimensional with x being the depth into the material. The first three equations have the form of the heat equation: on the left hand side is a time derivative and on the right is a second order spatial derivative. The first equation describes the change in temperature of the lattice by considering heat conduction and transfer of heat from the electrons to the lattice. In this equation $\rho$ is the material density, $C_L$ is the heat capacity of the lattice, T is the lattice temperature, $\kappa_L$ is the heat conduction of the lattice, $k_B$ is the Boltzmann constant, $n$ is the electron density, $T_C$ is the electron temperature, and $\tau_E$ is the electron relaxation time. The second equation is the change of plasma density by considering the gain in density by the

diffusion of electrons, linear and second order absorption, and the loss due to electron-hole recombination. In the second equation $D_\alpha$ is the diffusion coefficient, $\alpha_L$ is the linear absorption coefficient, I is the intensity, $hf$ is the energy of a single photon, $\beta$ is the two photon absorption coefficient, and $\tau_R$ is the electron-hole recombination time. The third equation describes the change in energy or temperature of the carriers within the plasma. The first term on the right hand side describes the change in carrier energy by their diffusion through the sample. In the third equation $U_C$ is the electron energy, $E_g$ is the band gap energy, and $\alpha_{FCA}$ is the free carrier absorption coefficient. The second term describes the energy the carriers have after excitation to the conduction band via absorption. The difference between the photon and band gap energy decides how high into the conduction band the electrons are, this means that these electrons can eventually participate in avalanche ionization. The third term is electron-hole recombination and the last term is the decrease in carrier energy due to transfer of energy to the lattice. The last equation is the spatial evolution of the intensity after considering single and two photon absorption as well as free carrier absorption. The authors of [13] used a square temporal intensity profile; over time the intensity of the pulse at a point is the same.

This system was solved using Matlab. The Forward Euler method was used for discretizing the problem in space and time. The method uses forward transfer time derivative and backward transfer spatial derivative [32]:

$$\frac{\partial T(x_i, t_{i+1})}{dt} = \frac{T(x_i, t_{i+1}) - T(x_i, t_i)}{\Delta t} \tag{3.10}$$

$$\frac{\partial T(x_i, t_i)}{dx} = \frac{T(x_i, t_i) - T(x_{i-1}, t_i)}{\Delta x}. \tag{3.11}$$

The derivatives in equations 3.10 - 3.13 are replaced with the finite difference derivatives and the element containing the future time i+1 at the current position i is isolated.

The Forward Euler method was employed in this calculation, because one can explicitly isolate for $T(x_i, t_{i+1})$. Although it is convenient computationally, it is subject to instability if the time step $\Delta t$ is too large. The instability grows and eventually approaches infinity as the calculation evolves temporally. In order to remain stable the quantity $\mathrm{v}\Delta t/\Delta x$ needs to be less than a critical value; v is the proportionality that relates the time derivative to the spatial one [32]. This stability condition puts a restriction on the accuracy of the solution; if the spatial step is reduced, the calculation may become unstable.

Input values of pulse duration, lattice, and electron temperatures were: $\tau = 70$ fs, I= $10^{13} W/cm^2$, $T_l = T_c$=300K, with initial carrier densities for N-type, intrinsic, and P-type:

n=$10^{16}cm^{-3}$, n=$10^{10}cm^{-3}$, n=$0cm^{-3}$. Although the laser system generates 40 fs pulses, 70 fs is used to account for pulse stretching as it propagates through the cube beam polarizer and other optical elements. According to the program, the maximum plasma densities reached by the three types is: n=$10^{23}cm^{-3}$, n=$10^{22}cm^{-3}$, n=$10^{12}cm^{-3}$, for N-type, intrinsic, and P-type respectively. The critical density of silicon is n=$10^{21}cm^{-3}$, therefore, the densities reached by N-type and intrinsic surpass this value and the over-critical behaviour described in [26] is observed. P-type on the other hand remains under critical and the under critical behaviour described in [26] is also observed in our results. The results of the program imply that the effect of the laser on N-type and intrinsic is the same since their maximum plasma densities are approximately the same. This similarity was observed experimentally in our study. The electron temperature as a function of time and depth is shown in Figure 3.17. The spatial scale on the left denotes the depth into the material in steps of 50 nm. It appears that the energy is absorbed primarily within the first 200 nm; the temperatures reach several thousand Kelvin depicted by the light blue and red. The short absorption depth agrees with the concept that the laser energy is concentrated with the skin depth of silicon which is much shorter than 1 $\mu$m [13]. The temperature will eventually decrease when the electrons begin to relax and transfer energy to the lattice, which occurs approximately 1 ps after the pulse impinges.

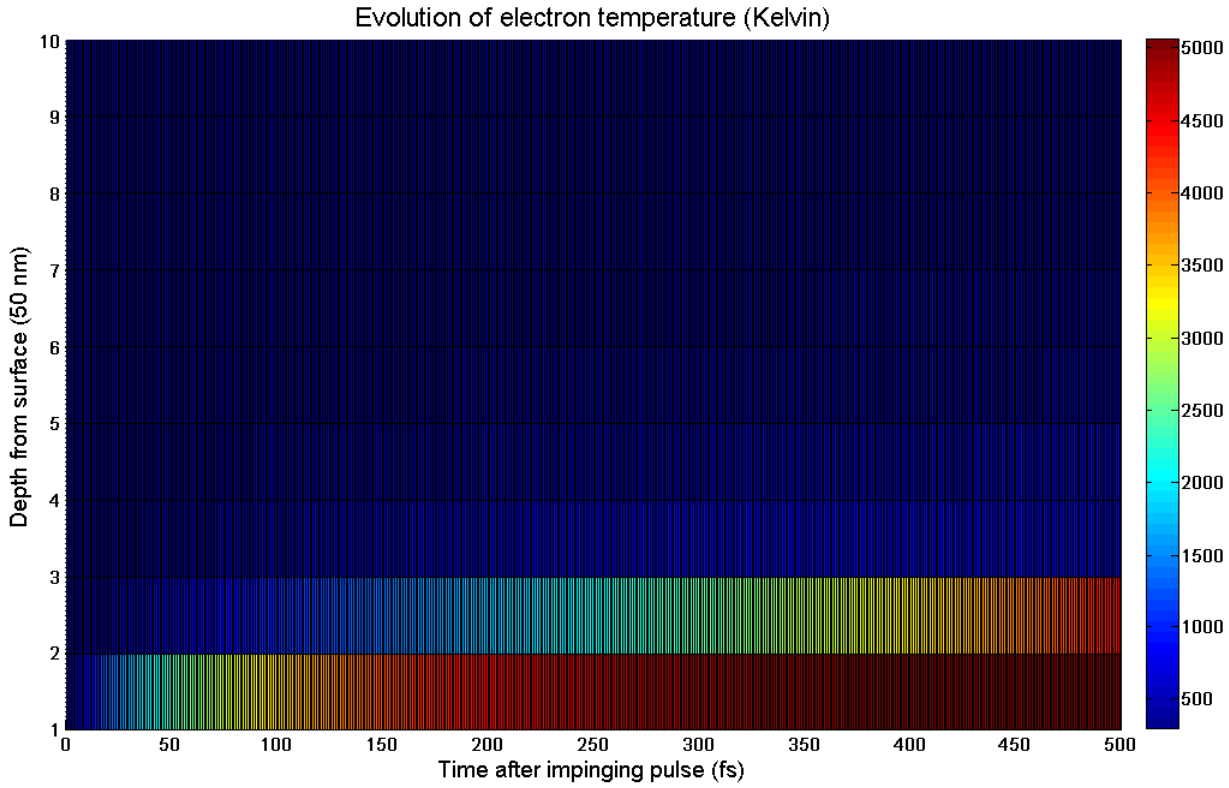


Figure 3.17: Electron temperature as a function of time and depth, calculated through the two-temperature model via equations 3.5 to 3.11.

## 3.5 Characterization of modified region

Material characterization by various methods is done, such as TEM, AFM, SEM, PL, electron diffraction, etc., to give information about the topology, electronic structure, etc., of the sample. Through surface material characterization such as SEM and AFM, physical observations of the modified sample are collected. These physical observations can be combined with the chemical and optical observations made by PL, TEM, and electron diffraction to gain an understanding of the modification.

### 3.5.1 Transmission electron microscopy and electron diffraction

Figure 3.18 is a transmission electron microscope image of a slice through a structure formed by a $1.0 J/cm^2$ pulse with 55 nJ. The image shows a cross section of the structure;

the bumps in Figure 3.18 are from the ring and the crater is the valley between them. A focused ion beam using $Ga^{2+}$ ions was used to create a thin cross section of a single pulse structure. The sample was coated with carbon and then titanium to prevent the surface from being damaged by the focused ion beam. Lines across the sample are Kikuchi lines, which show the bands of electron scattering. The bands connect the intersections of the crystallographic planes, hence they appear in thick samples. They show the locations of multiple scattering events [33].

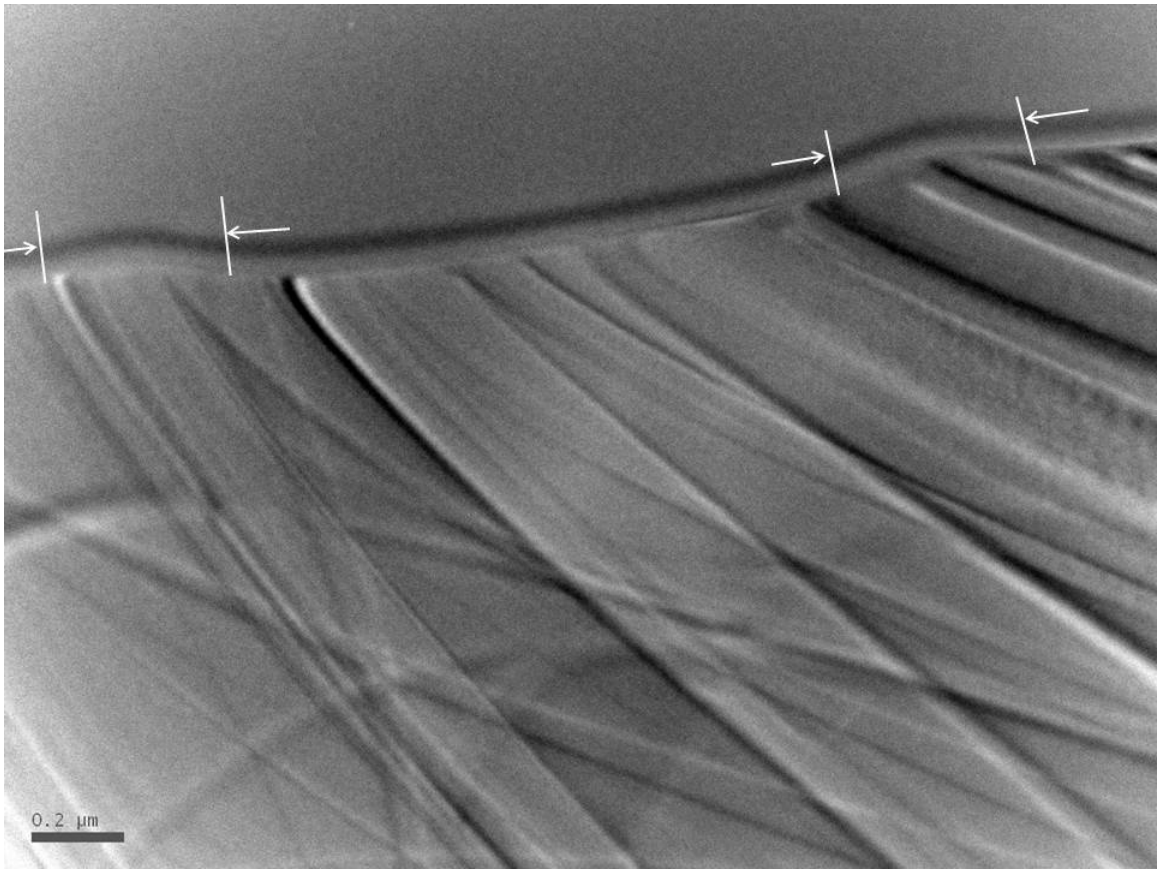


Figure 3.18: TEM image of slice. The arrows point to the rims that surround the crater. The lines within the bulk are due to Kikuchi diffractions.

Electron diffraction was performed on the TEM slice to investigate if and how the crystallinity of the modification changed. Figure 3.19 is the pattern generated for pristine silicon, 2 $\mu$m below the surface. It was performed at an arbitrary depth that is much greater than the skin depth to ensure there was no laser modification to the region. The main, undiffracted electron beam is blocked after the sample so that only the diffracted

electrons reach the detector; the pattern is composed only of the diffracted electrons. The diffraction pattern in the figure demonstrates that the lattice is composed of a single crystal pattern because the peaks are spread throughout the image, which means there is long range periodicity. A peak occurs wherever the scattered electron waves constructively interfere. The electron beam will scatter from the electron density surrounding each atom and will constructively interfere, if the Bragg condition is fulfilled. Higher order peaks have a reduced amplitude as a consequence of multiple scattering events.

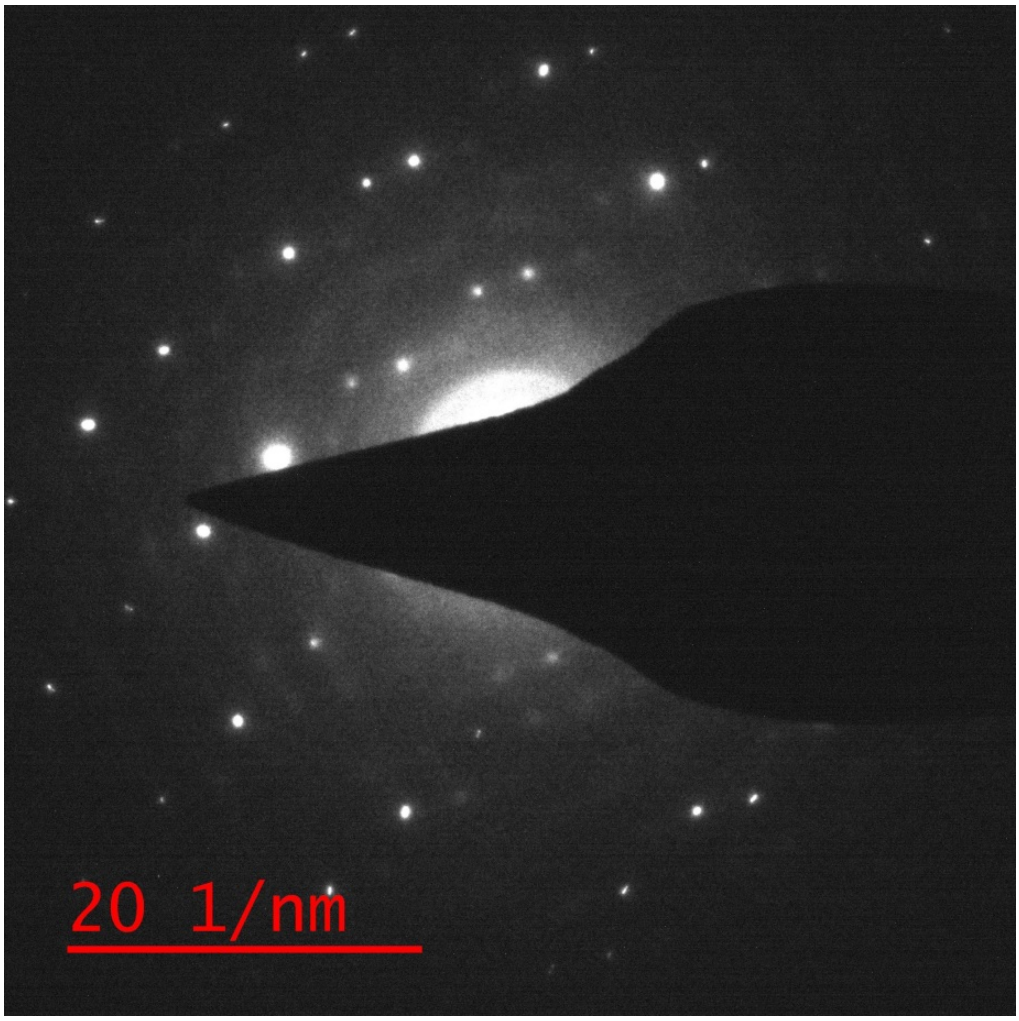


Figure 3.19: Electron diffraction of unmodified silicon, 2 $\mu$m below the surface.

Figure 3.20 is the pattern generated when the electron beam was incident at the rim or just below the crater; the figure shows the pattern at any modified point. In comparison to Figure 3.19, there are fewer high order peaks, which indicates that the material has become polycrystalline. Polycrystalline materials have domains of crystallinity. Therefore, constructive interference of scattered electron waves is limited to a domain and hence no higher order peaks are observed. The rings formed in the centre of the patterns in both figures is due to the milling process [25].

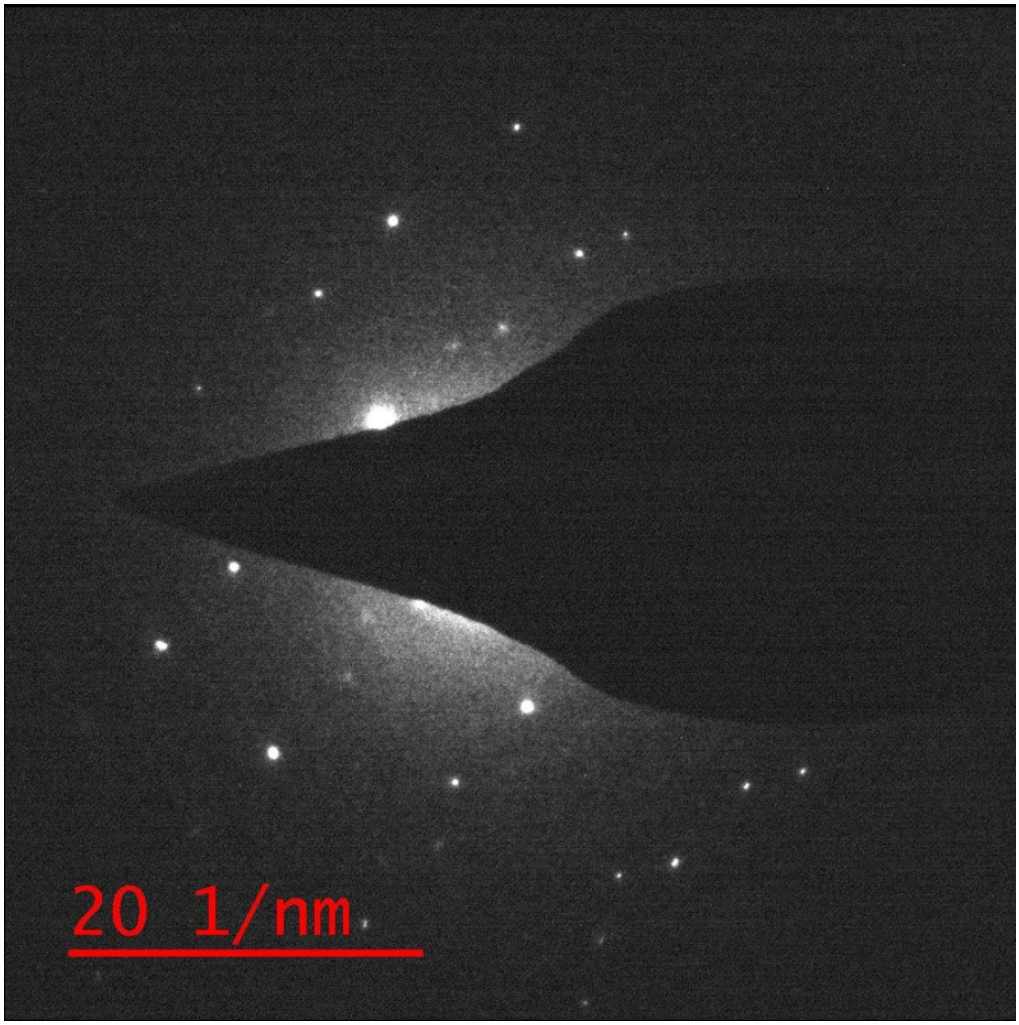


Figure 3.20: Electron diffraction of the single pulse structure.

### 3.5.2 Photoluminescence

Photoluminescence (PL) spectra display all fluorescence and emission spectra of the excited region. It is a general term used for spontaneous emission of light after the surface has been photo-excited. Depending on the excitation wavelength different electronic states will be excited, therefore it gives information about the electronic structure. For surface microstructuring PL data is useful, because the signal is coming primarily from the surface when the excitation wavelength is above the band-gap. Therefore, PL is sensitive to differences between the structured and unstructured surfaces. Major differences to note are the differences in their peak emissions as well as their relative intensities. In this study PL were collected from the unmodified (Figure 3.21) and modified (Figure 3.22) regions to observe any differences between their emissions. The samples were excited from 750 to 880 nm in an increment of 10 nm. Figure 3.21 shows that the emission of the photoluminescence spectrum is centred around 1140 nm for the unmodified region. It is observed that the intensity of the emission increases with increasing excitation wavelength. The energy of the emission is 1.09 eV, which is nearly equal to the 1.1 eV band-gap of silicon. Due to the fact that linewidths have Lorentzian profiles [27], there is a range of frequencies that can promote electrons from the top of the valence band to the bottom of the conduction band. Therefore, the 1.09 eV emission is caused by the recombination of an electron in the conduction band with a hole at the top of the valence band [34].

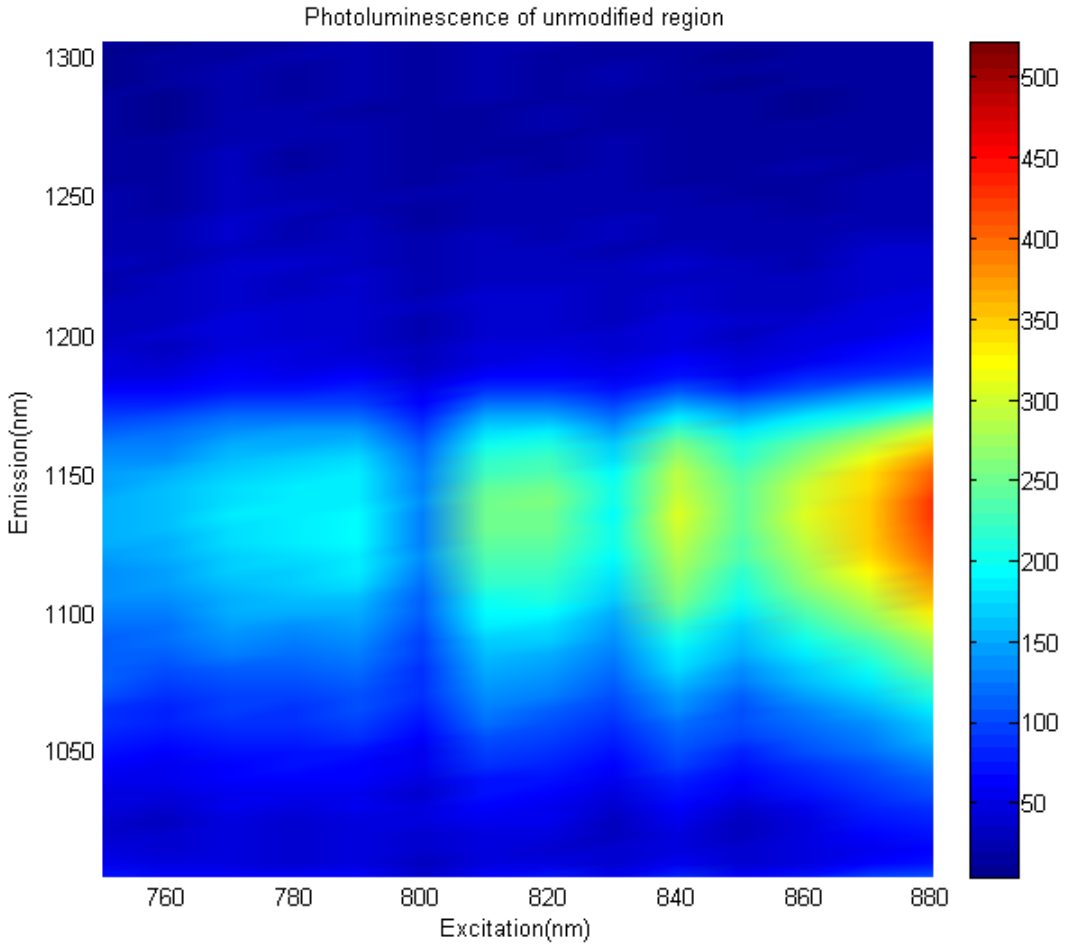


Figure 3.21: Photoluminescence of unmodified silicon

The intensity of the modified emission is greater than the unmodified as displayed in Figure 3.22 and more convincingly in Figure 3.23. This increase can be explained in conjunction with the electron diffraction data. According to Figures 3.19 and 3.20 laser irradiation caused the material to become slightly amorphous or polycrystalline. This change in crystallinity may also result in a change in the electronic structure possibly by modifying the band structure. In [35] the authors related changes in PL signal to changes in depletion thickness, which is the maximum thickness for receiving PL signal. It can change, if there is bending in the electronic states around the band-gap. Differences in the PL spectra for modified and unmodified silicon is still under investigation.

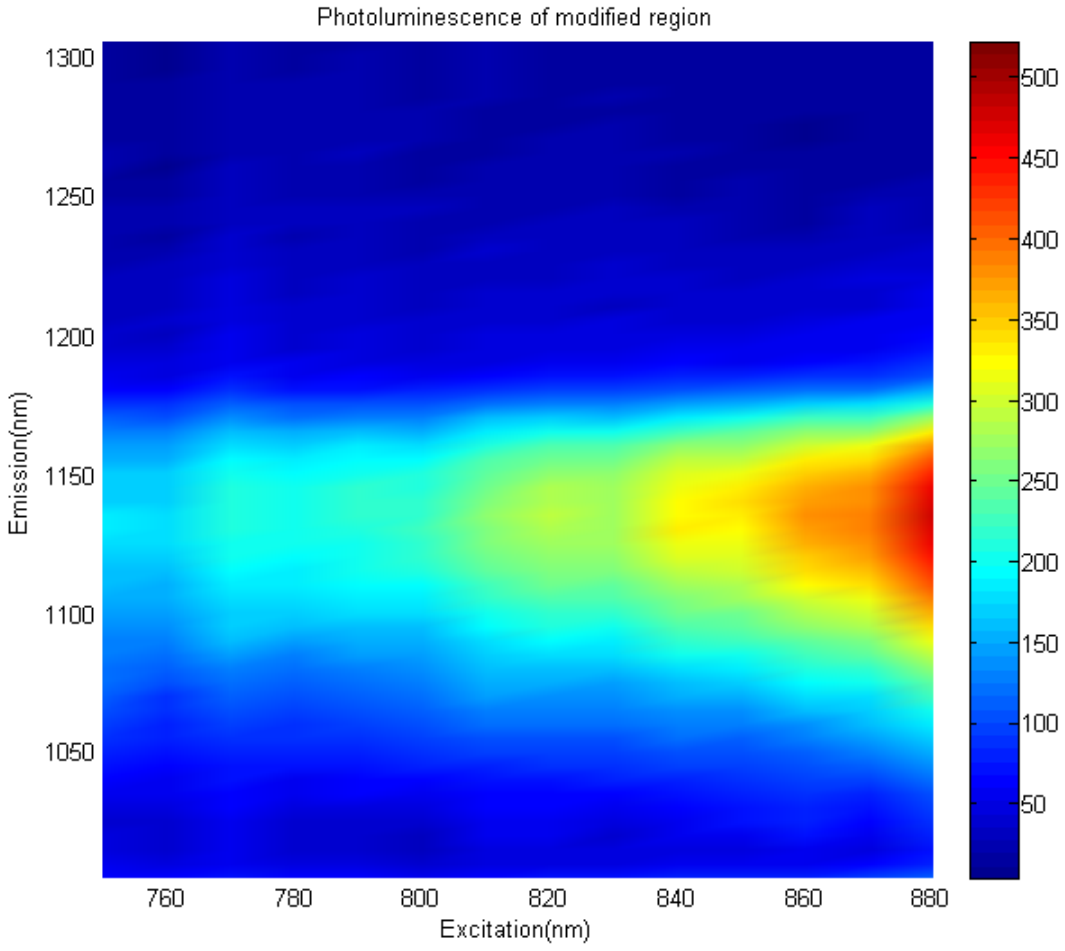


Figure 3.22: Photoluminescence of modified silicon

Figure 3.23 displays the peak emission wavelength for modified and unmodified silicon as a function of excitation wavelength. The peak for both spectra occurs at 1140 nm. For the entire excitation range the intensity of the modified is greater than the unmodified.

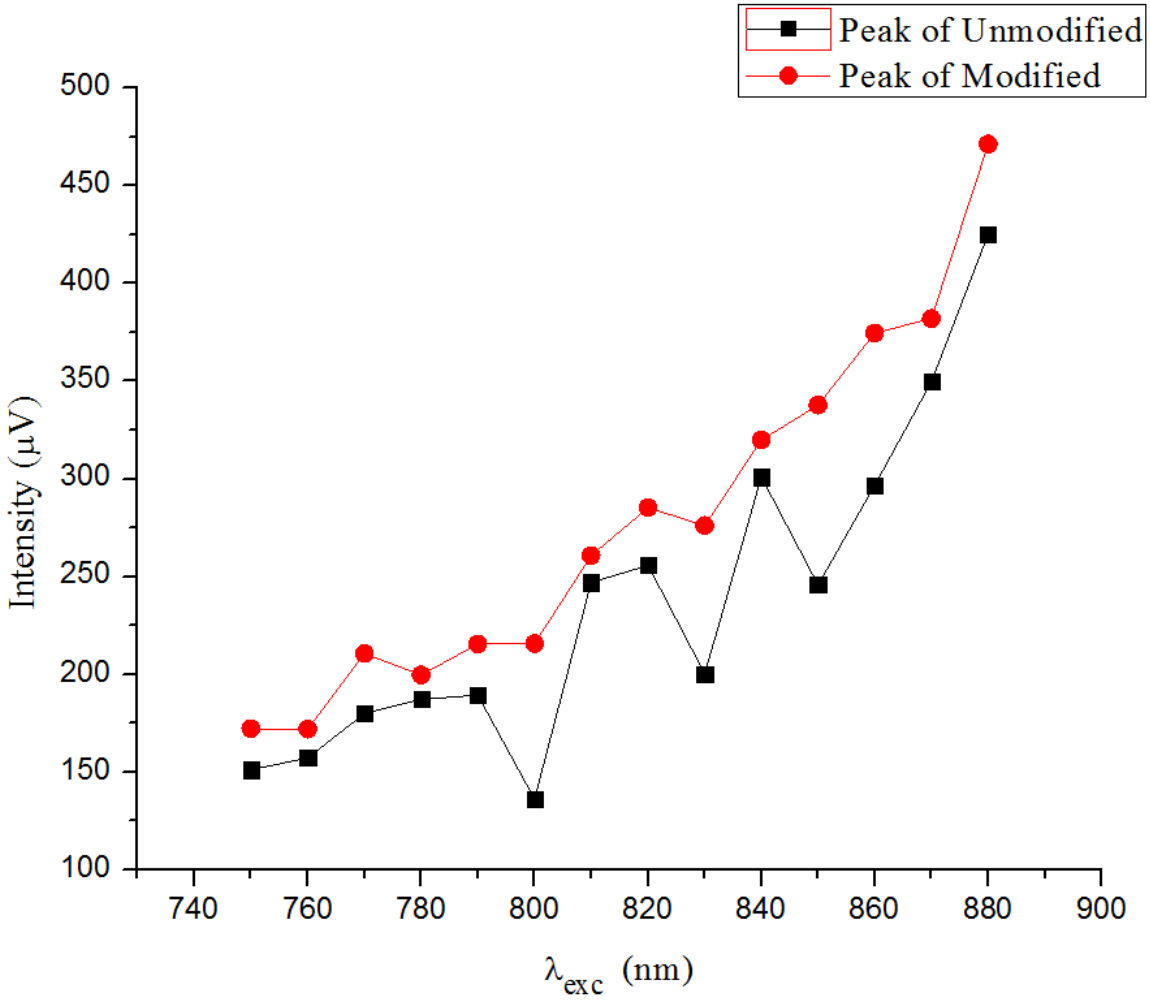


Figure 3.23: PL peaks for modified and unmodified silicon occur at approximately 1140 nm. Displayed in this figure is the intensity of the peak as a function of excitation wavelength.

Figures 3.24, 3.25 and 3.26 are cross sections of Figures 3.21 and 3.22. The cross sections are taken at the excitation wavelengths that correspond to minima in the unmodified spectrum of Figure 3.23.

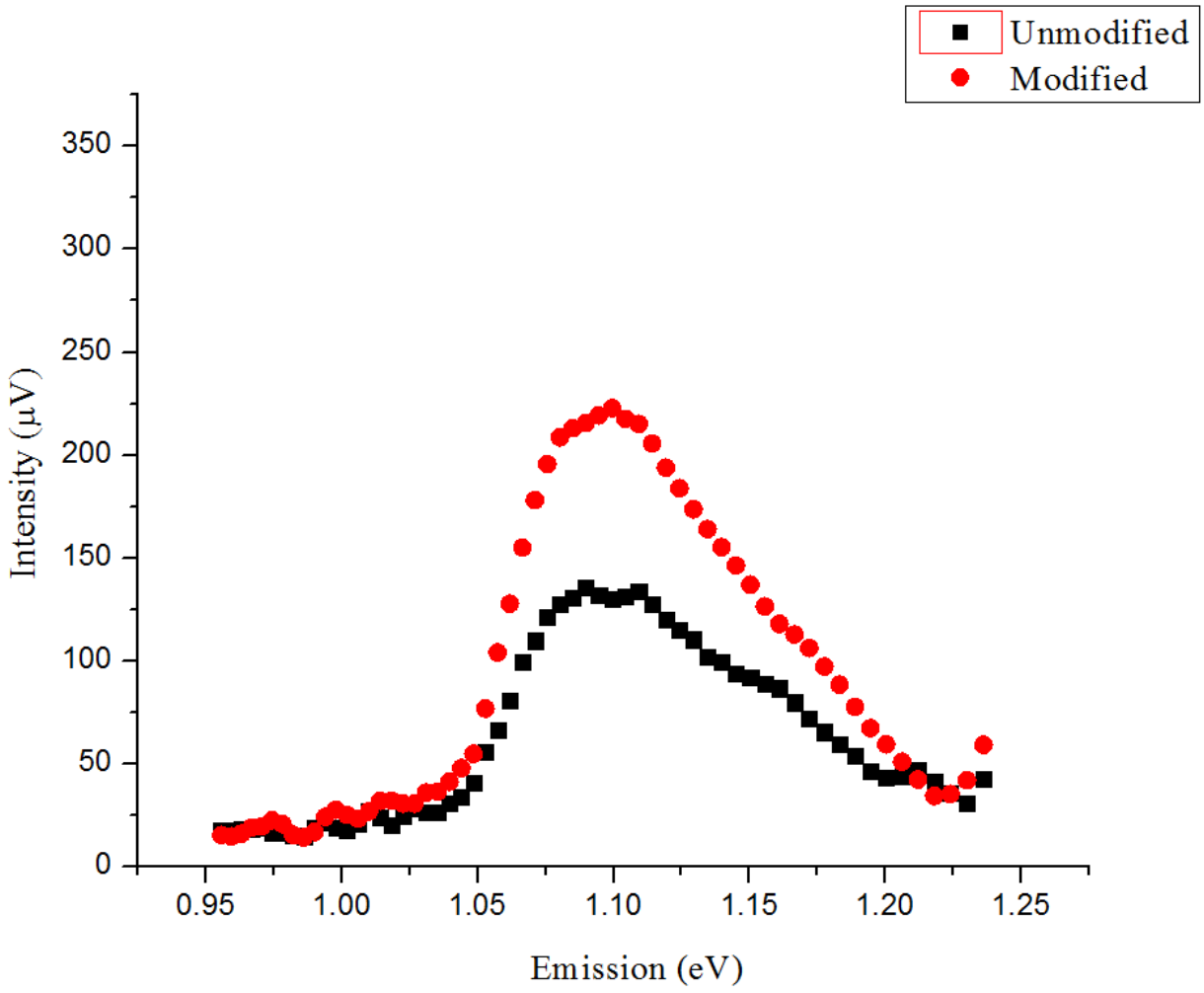


Figure 3.24: PL intensity of modified and unmodified silicon as a function of emission wavelength for excitation wavelength 800 nm. FWHM's for modified and unmodified are 0.1 and 0.11 eV.

There appears to be a shoulder on the right hand side in the PL spectrum when the samples are excited with 800 nm in Figure 3.24. It was explained in [34] that a shoulder is present because of the necessity for the generation of phonons to conserve momentum since silicon has an indirect band-gap. The presence of the shoulder results in the larger

FWHM compared to the other excitation wavelengths, which unanimously have 0.09 eV.

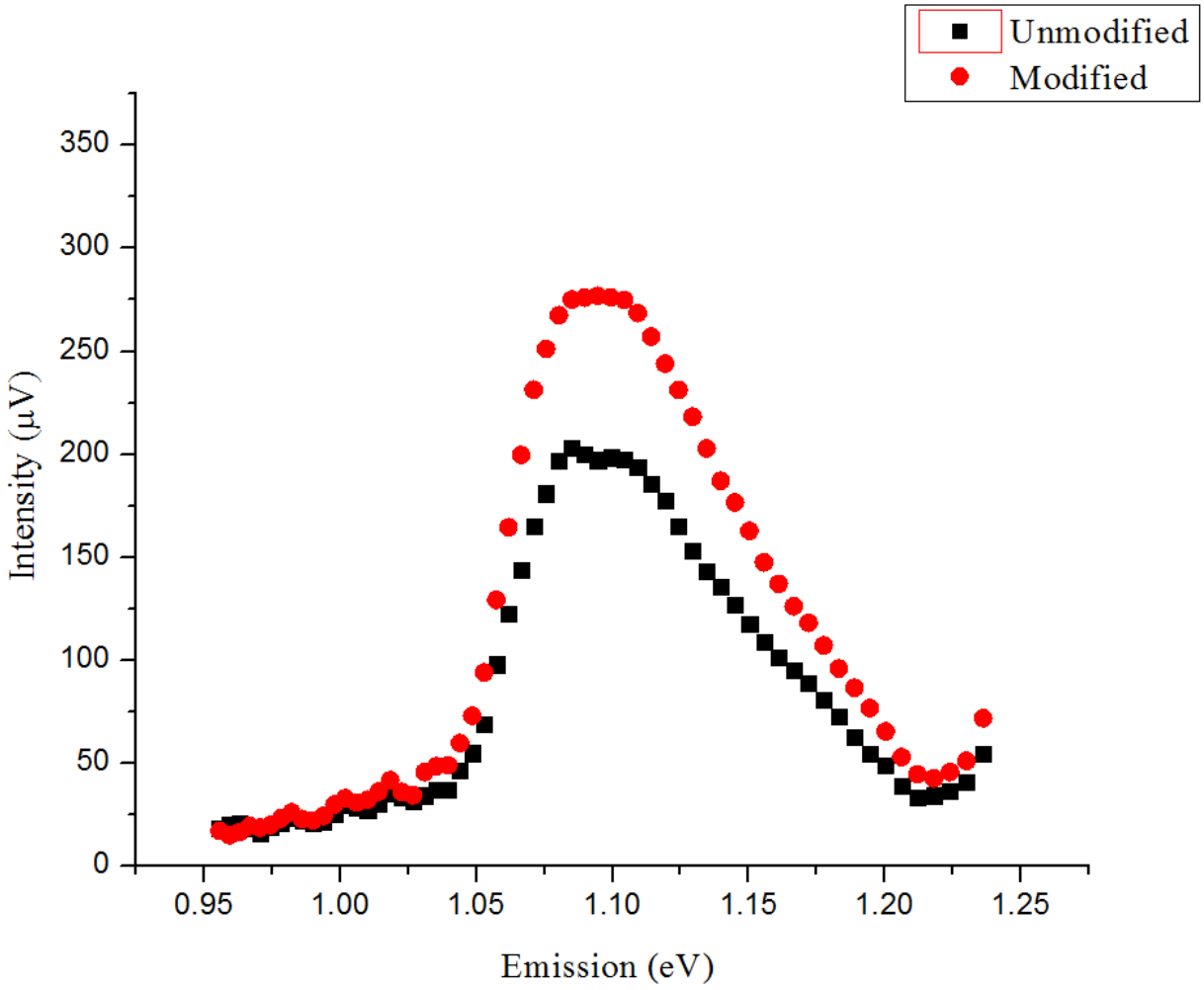


Figure 3.25: PL intensity of modified and unmodified silicon as a function of emission wavelength for excitation wavelength of 830 nm. FWHM's for modified and unmodified are 0.09 and 0.09 eV.

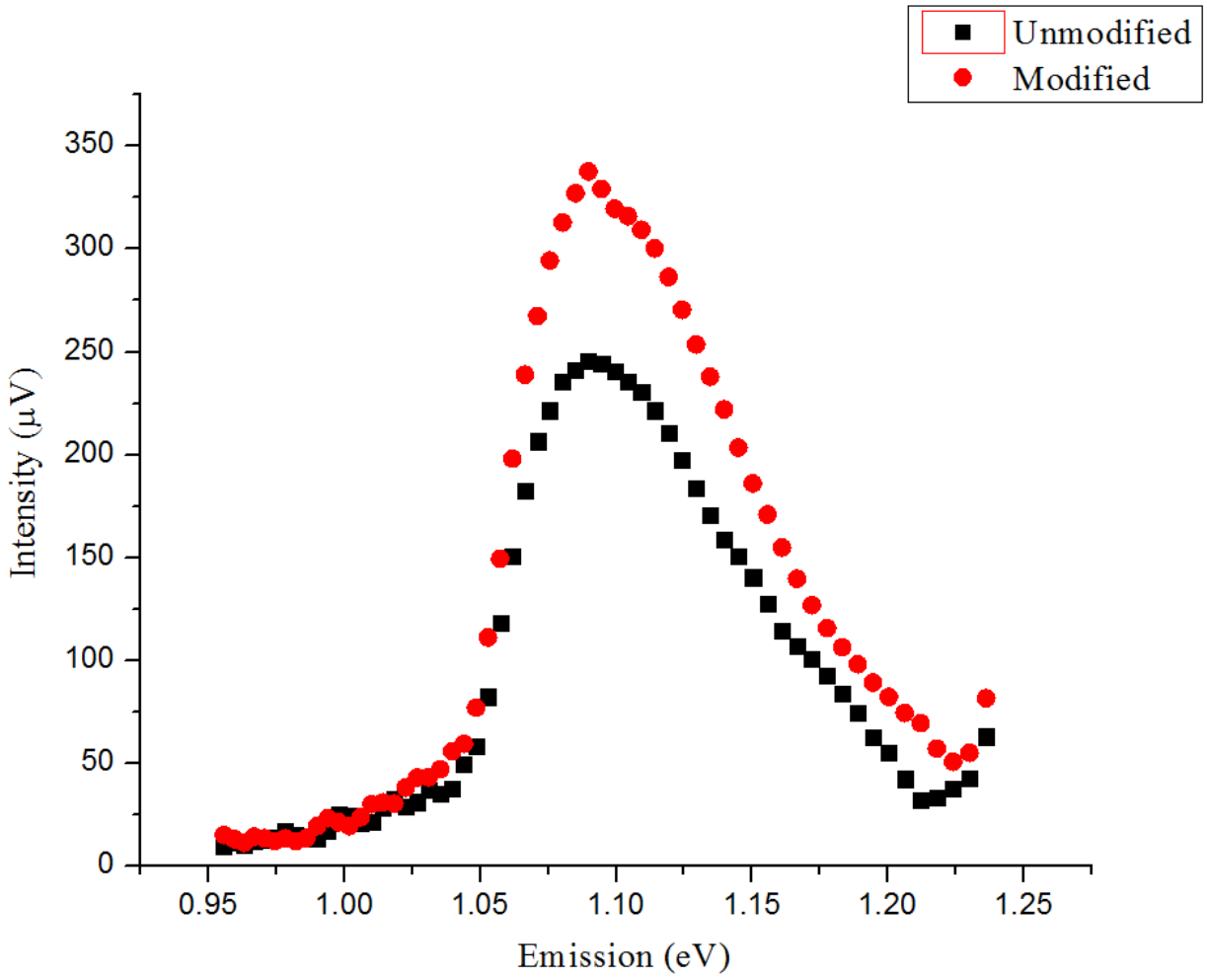


Figure 3.26: PL intensity of modified and unmodified silicon as a function of emission wavelength for excitation wavelength of 850 nm. FWHM's for modified and unmodified are 0.09 and 0.09 eV.

Concluding, the single pulse structure consists of a crater surrounded by a raised rim on the surface. It was observed that the dimensions of the structure: width, diameter, height, and depth, (Figures 3.7, 3.8) increase with energy. The distinctive feature is the height asymmetry of the ring that is attributed to field enhancement. Unlike for femtosecond laser ablation of dielectrics such as PMMA [26], the elongation in the structure is observed in the ring height as opposed to the diameter.

# Chapter 4

# Multiple pulse observations

For industrial applications, ablation is primarily performed by irradiating the target with multiple pulses. For instance in [10] several hundreds of pulses were used to create the conical structures that increase light absorption of solar cells. In our multiple-pulse study we focused on the fundamental aspect, thus the evolution of structures with number of pulses was explored. We studied only N-type silicon in our experiments and varied the number of pulses from two to five. The time delay between the pulses was determined by the repetition rate of the laser. The single pulse structure explored in chapter 3 is the topology experienced by the subsequent pulses. The first section presents the multiple-pulse observations and the second section explores the polarization dependence.

## 4.1 Multiple pulse structures

Figures 4.1 - 4.6 show the multiple pulse structures for 2 - 5 pulses. In these figures the orientation of the electric field is pointing to the top and bottom of the page ↕.

### 4.1.1 Two-pulse

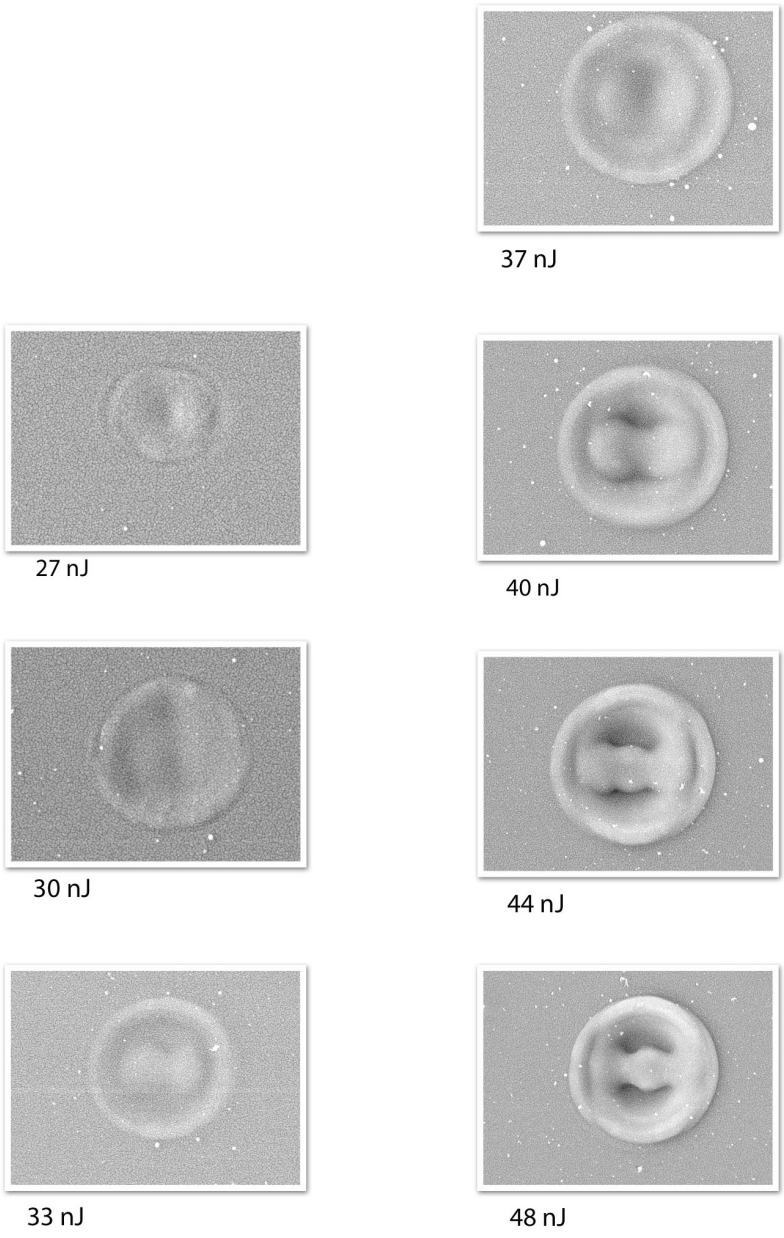


Figure 4.1: SEM images of two-pulse structures from 27 - 48 nJ with the electric field pointing ↕.

The two-pulse structure will now be discussed. Referring to Figure 4.1, the dimen-

sions of the structure increase with fluence as expected. In addition, a double rim forms perpendicular to the polarization, which can be discerned by the contrast in the image. Within the crater there is more material removed along the polarization, and this difference in the crater shape becomes more enhanced as the fluence increases.

The view of the structure perpendicular to the electric field looks like the single pulse as shown in red in Figure 4.2. The red profile also shows that there is a double rim surrounding the crater that is attributed to the piling up of particles at the cold boundary after each pulse. However, the view parallel to the polarization, shown in

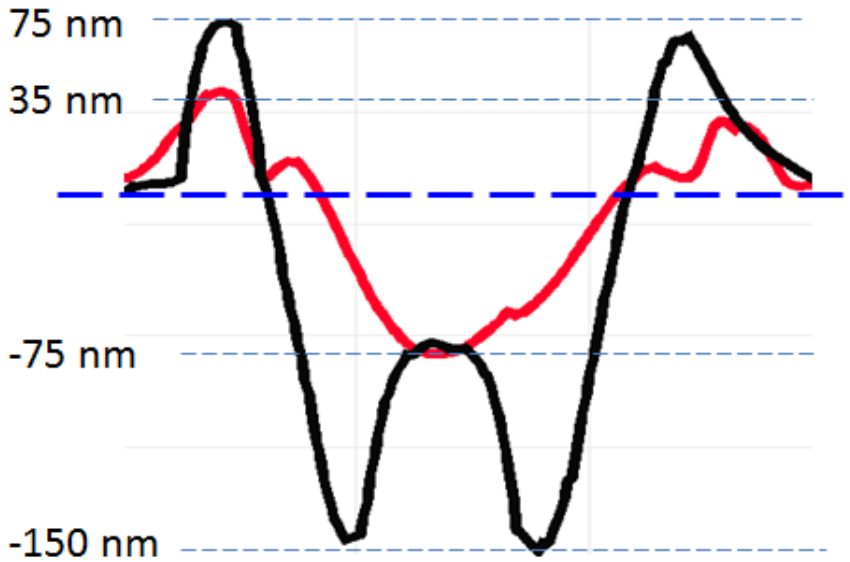


Figure 4.2: Profiles of two pulse structure as seen along and perpendicular to the electric field, created with a pulse of 44 nJ.

black in Figure 4.2, shows that the crater has a raised center resembling a tooth. A three dimensional AFM image of the structure is shown in Figure 4.3. The image was oriented to emphasize the height asymmetry and the tooth-like structure of the crater. The asymmetry of the ring heights in 4.2 is approximately 2, which is greater than all of the height asymmetries calculated in Chapter 3. Based on these observations it appears that the second pulse acted to amplify the polarization dependent features. Even though the plasma density gradient is the same for the second pulse as it is for the first, the motion of particles is different. For the single pulse the most energetic particles are simply moved radially outwardly as they cool until they encounter the cold boundary

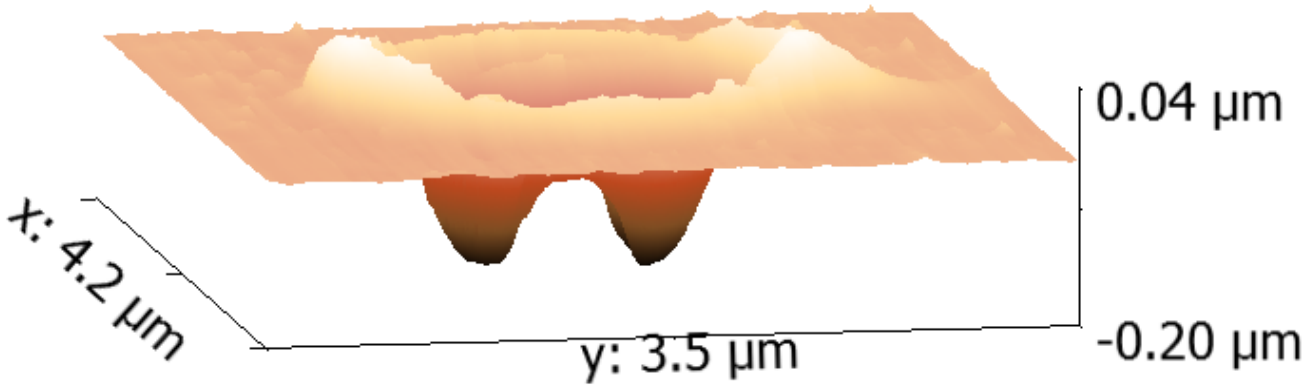


Figure 4.3: This structure was created with a pulse of 44 nJ.

and abruptly stop. For two pulses the structure may be explained by considering the fact that the motion of the hydrodynamic wave is influenced by the topology of the already structured surface since the geometry of the plasma depends on the topology. The expanding hydrodynamic wave reflects from the walls of the crater. At the bottom of the crater the returning particles merge to form the protruding structure along the polarization as shown by Figures 4.1 and 4.2. Due to field enhancement the high kinetic energy of particles along the polarization enables them to go up and then come down again before solidifying. Whereas particles orthogonal to the polarization solidify as they move up. The multiple pulse structure is still under investigation.

### 4.1.2 Three, four, and five-pulses

Figures 4.4, 4.5, and 4.6 show the structures formed by three, four, and five pulses. The multiple-pulse experiments were performed with pulses separated by the 1 kHz repetition rate of the laser. Thus, the single pulses were separated by 1 ms, which is longer than the electron and phonon relaxation processes [11]. After transferring energy to the lattice the plasma no longer exists so there is no interaction of the field of the next pulse with the plasma generated by the previous pulse. Instead, successive pulses interact with the modified surface. The process of formation of multiple-pulse structures shown in Figures 4.1-4.6 is similar to that of the single pulse: pulse impinges on the surface, ionizes the material within the skin depth forming plasma, and transfer of heat to the lattice causes motion of particles due to hydrodynamic pressure. Therefore each subsequent pulse after the first interacts with the new topology of the surface morphed by the previous pulses. The main difference between the multiple-pulse regime and the single pulse regime is that the geometry of plasma differs, because it forms along the structured surface which is no longer flat.

In Figure 4.4 there is a protruding structure from the centre of the crater that surpasses the rim in height. For Figures 4.5 and 4.6 there appears to be explosive ablation or material removal around 40 nJ. Before this stage, for the three and four pulses of Figures 4.4 and 4.5, there is a clear ordering of the internal structures at 37 nJ. This vivid ordering is also observed for the five pulse structures in 4.6 before explosive ablation at 33 nJ. For the five pulse structure there also appears to be distinct ordering in the explosive ablation regime above 33 nJ; this is not as obvious for the four and three pulses. Several references were mentioned in this thesis that discussed the formation and observations of laser induced periodic surface structures (LIPSS) [18–20]. LIPSS are primarily a multiple-pulse phenomenon and it is possible that the ordering of structures is due to the same mechanism. Understanding the multiple-pulse structures is still incomplete and verifying the applicability of this theory must still be done.

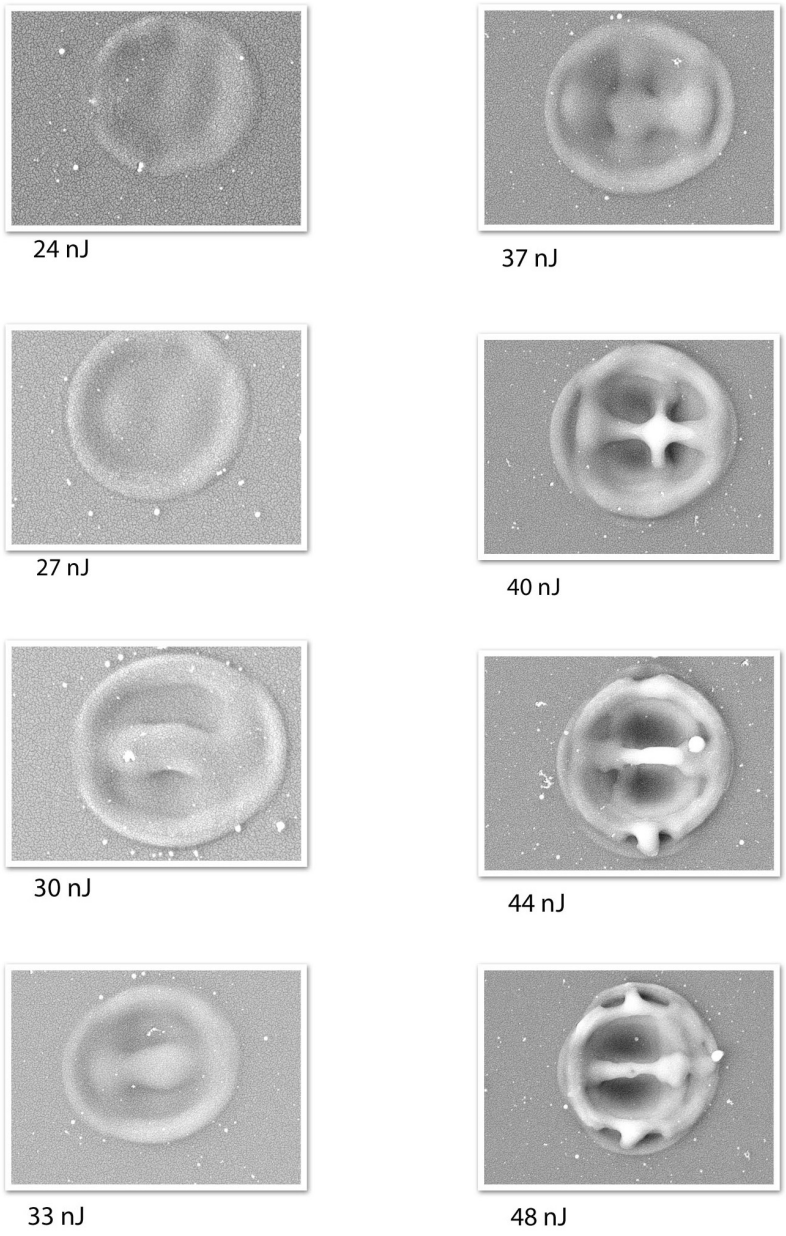


Figure 4.4: SEM images of three-pulse structures from 24 - 48 nJ with the electric field pointing ↕.

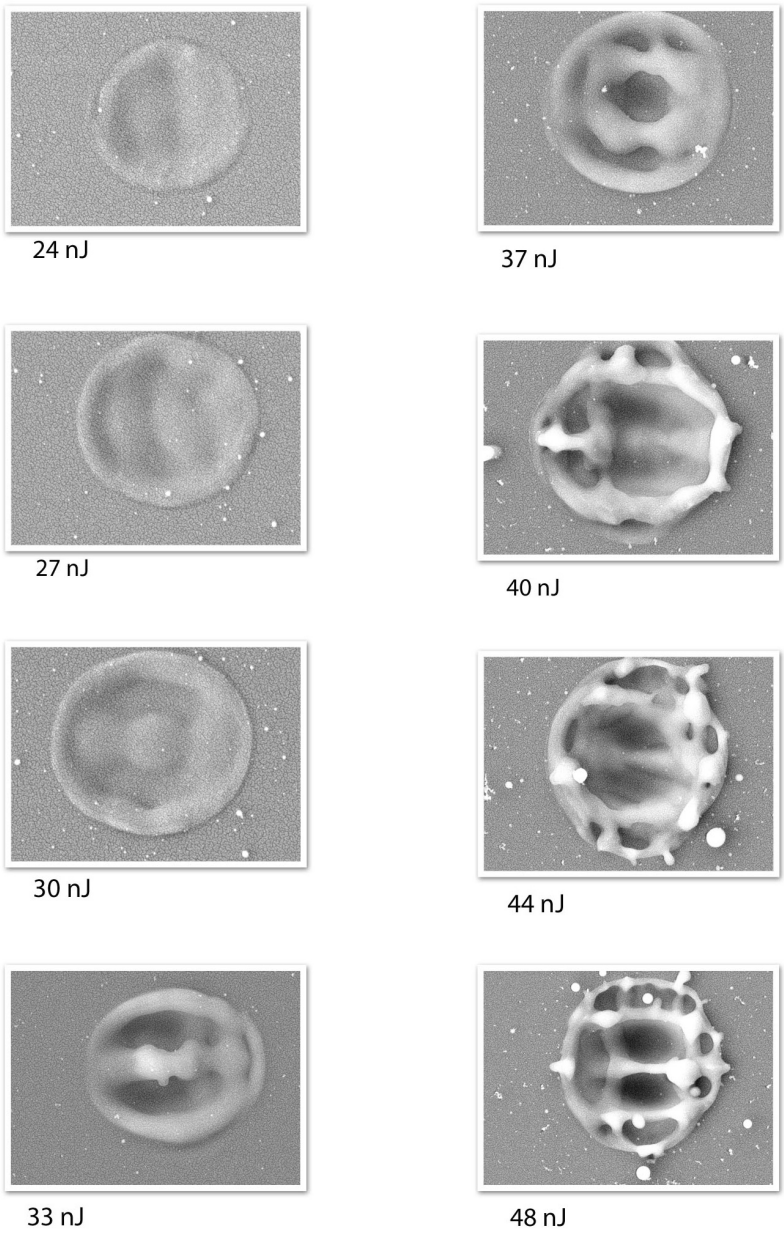


Figure 4.5: SEM images of four-pulse structures from 24 - 48 nJ with the electric field pointing ↕.

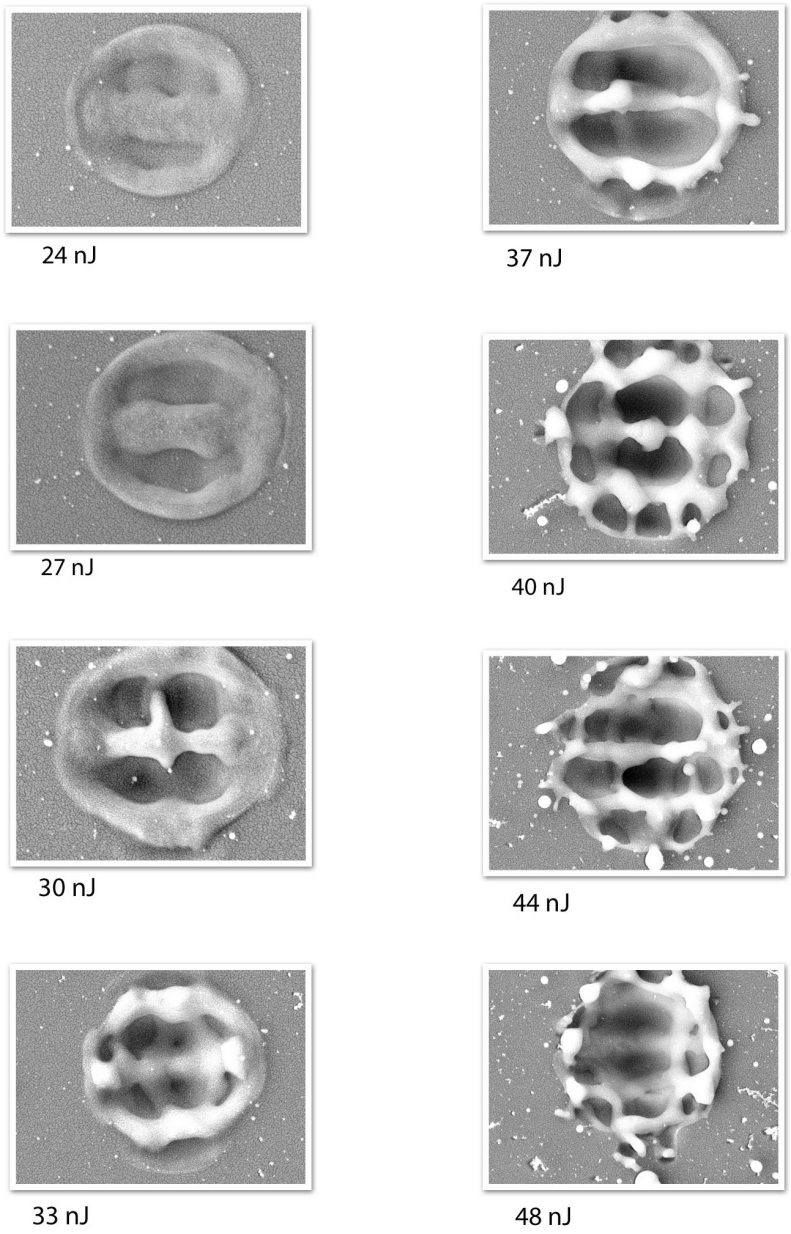


Figure 4.6: SEM images of five-pulse structures from 24 - 48 nJ with the electric field pointing ↕.

## 4.2 Polarization effects

Figures 4.7, 4.8, and 4.9 display the linear and elliptical polarization structures for two and three pulses. The energy of all the figures is about 40 nJ and peak fluence is $0.9 J/cm^2$.

In Figure 4.7, (a, b) are the two-pulse and (c, d) are the three-pulse structures. $0^0$ corresponds to the vertical and $90^0$ to the horizontal orientation of the electric field. The internal structures within the crater completely change their orientation with the change of the electric field. In all the images there is a line of raised material created perpendicular to the field. Figure 4.8 shows the two-pulse dependence on elliptical polarizations. The ellipticity of the polarization is written below the images in degrees. Figure 4.8 a is left circularly polarized and d is right circularly polarized. It appears from these images that there is a central protrusion and the surrounding material is pushed radially outwardly forming a concentric ring. Just as in the linear case shown in Figure 4.1, there appears to be a double rim most likely caused by the overlapping of the rings of subsequent pulses. By comparing Figure 4.8 a, d with the remainder of the images one observes that the internal structure elongates with increasing ellipticity so that it stretches across the crater and no longer is isolated to the centre. The field of image 4.8 c is actually linear since the whole beam rotated by $90^0$. It is clear in this image that the radial symmetry found in images a and d is lost. The dependence of concentricity on the degree of ellipticity in Figure 4.8 demonstrates that the motion of material follows the orientation of the field.

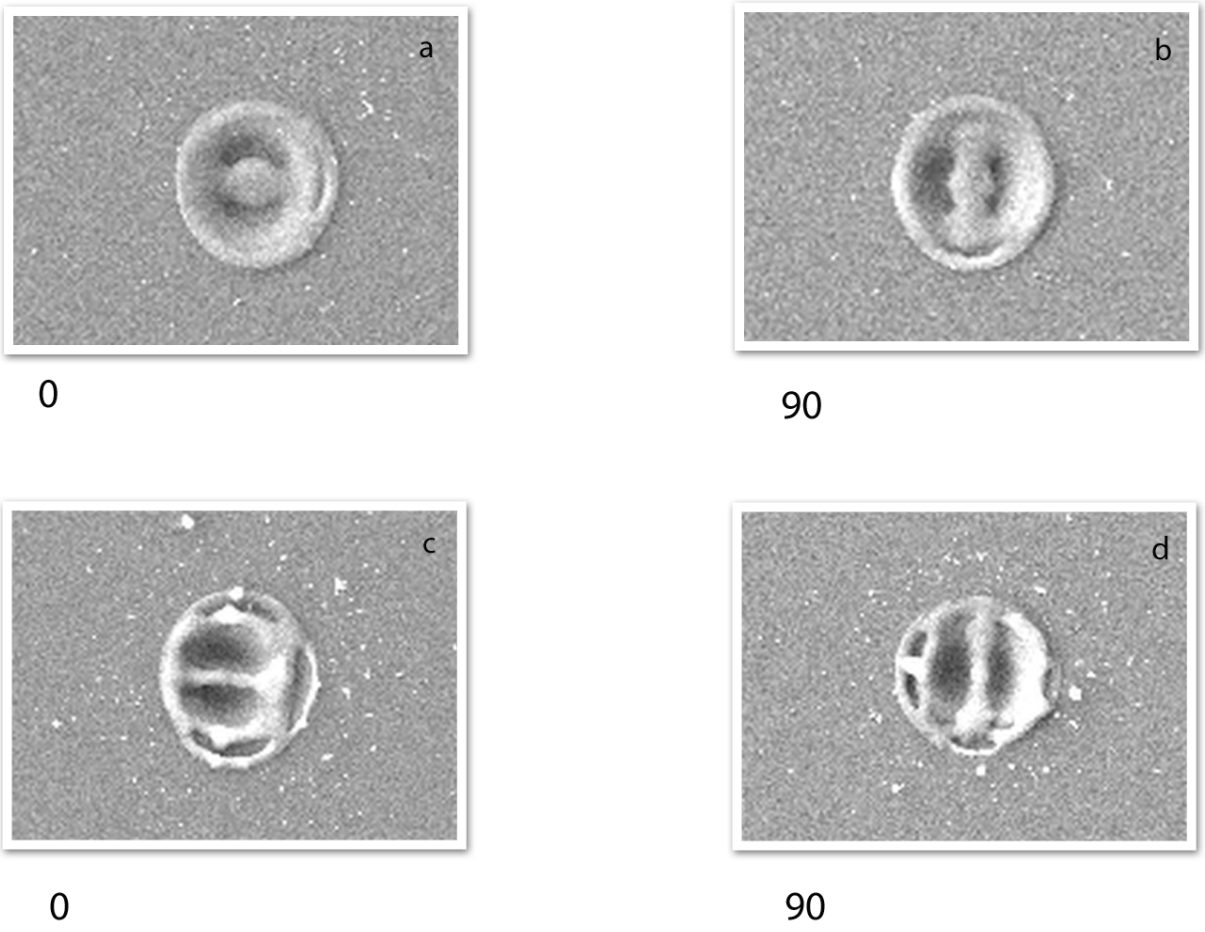


Figure 4.7: SEM images of two (a, b) and three-pulse (c, d) structures with different linear polarizations. The angles of the half waveplate is written in degrees below each image.

Similar observations are made with the three-pulse structures of Figure 4.9 as Figure 4.8; however the polarization dependence is more pronounced. For instance, the central protrusion for both circular orientations appears to be taller; there is a larger contrast in the brightness of the image in comparison to the centres of Figures 4.8 a and d. According to the hypothesis presented in section 4.1, each impinging pulse after the first moves some material to the centre by reflection from the crater wall. Therefore, it is expected that the protrusion would increase with the number of pulses because the amount of mass moved to the centre is compounded.

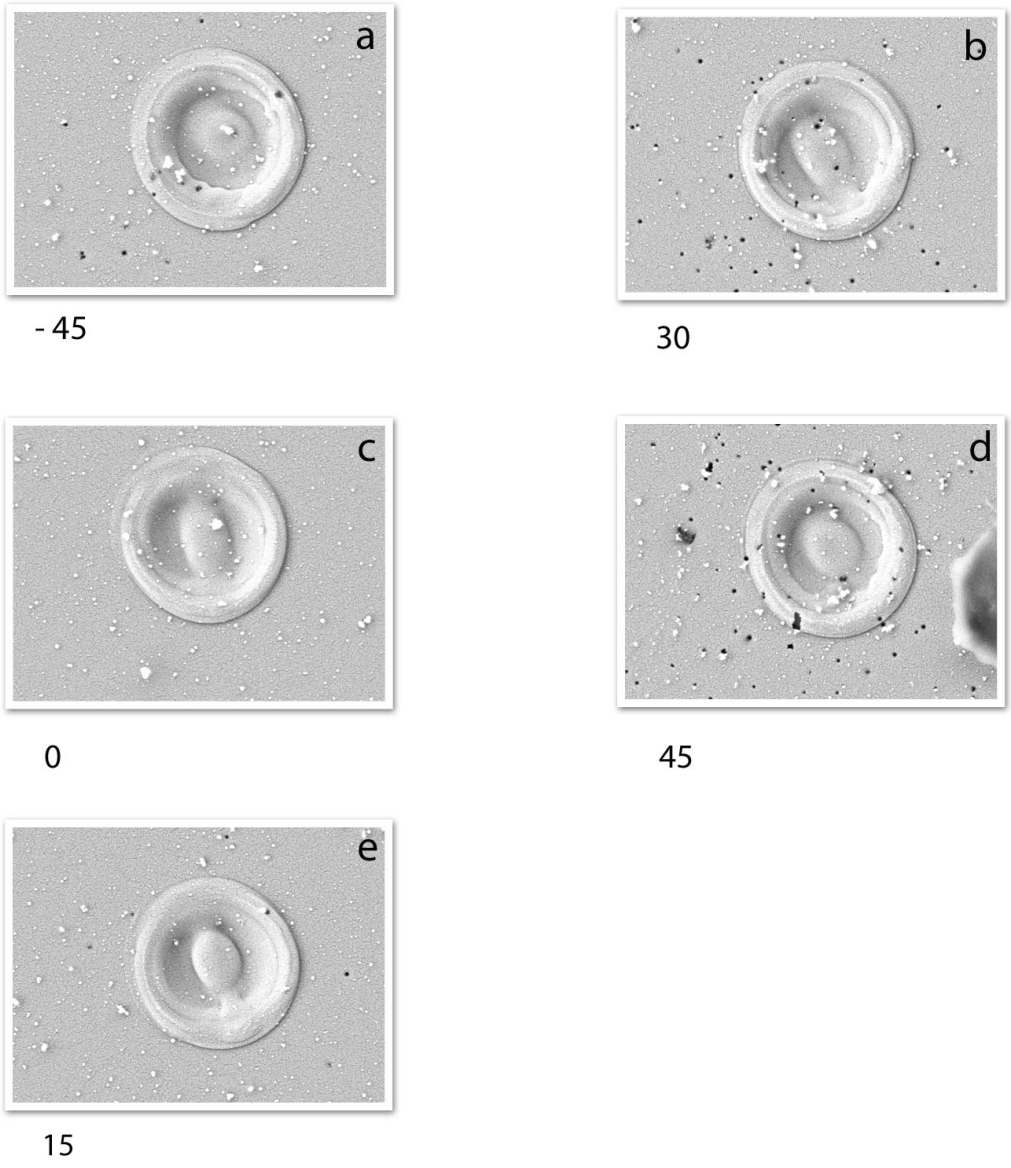


Figure 4.8: SEM images of two-pulse structure with elliptically polarized light, the angle of rotation of the quarter waveplate is written at the bottom of each image. Left circularly (-45$^0$), linearly (0$^0$), right circularly (45$^0$), and (15$^0$) and (30$^0$) are elliptically polarized.

Multiple pulse structuring in our studies has shown that there are internal structures formed within the crater and the polarization effects become more pronounced with increasing pulses. Protruding structures also increase in height with increasing energy.

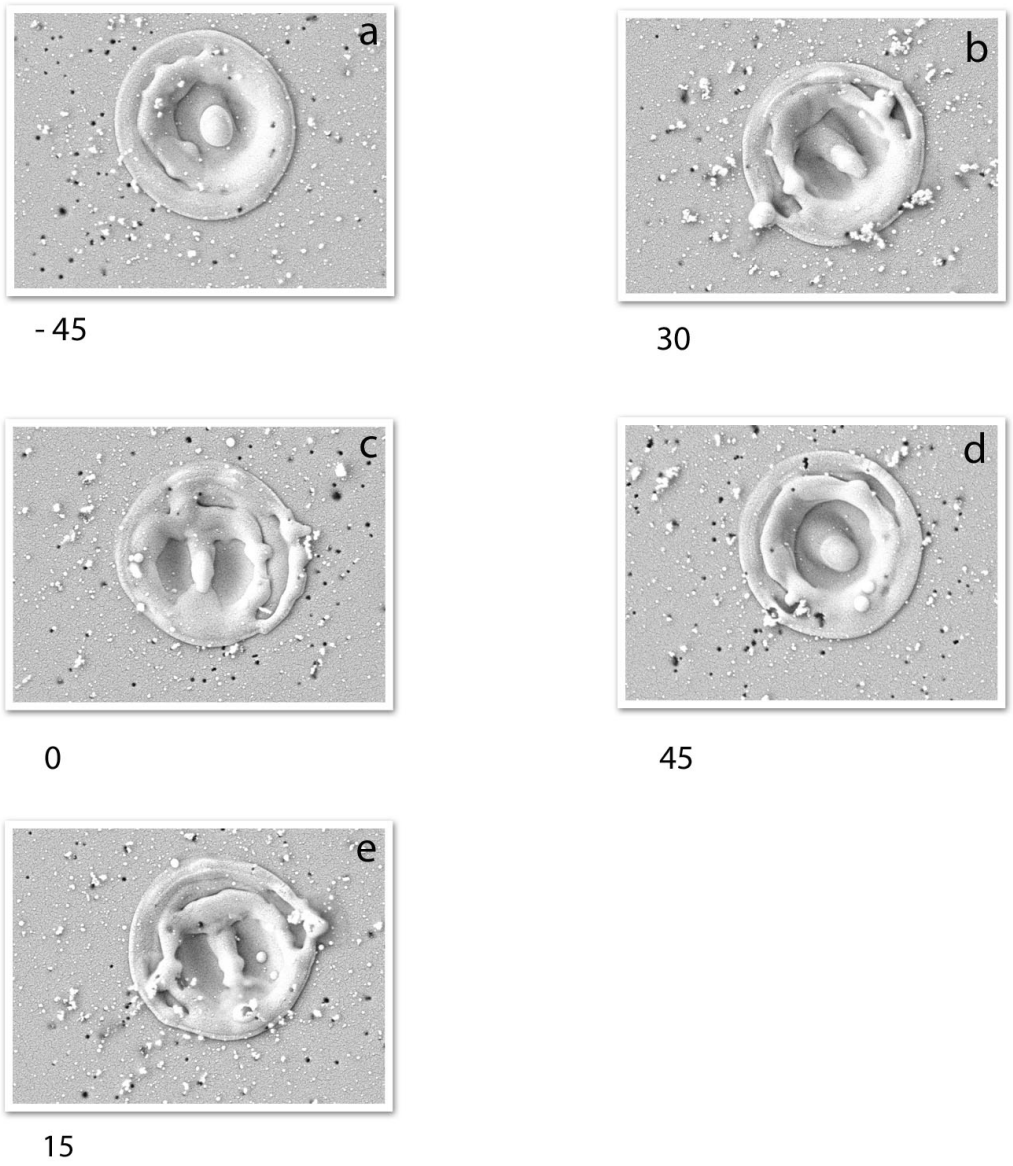


Figure 4.9: SEM images of three-pulse structure with elliptically polarized light, the angle of rotation of the quarter waveplate is written at the bottom of each image. Left circularly (-45$^0$), linearly (0$^0$), right circularly (45$^0$), and (15$^0$) and (30$^0$) are elliptically polarized.

An ordering of the internal protrusions also appears to increase with energy that is linked to LIPSS formation.

# Chapter 5

# Conclusions and Future Work

## 5.1 Summary and conclusion

The ring-like structure of the single pulse is formed when the hydrodynamic wave expands until it abruptly stops when it reaches the cold boundary of the non-irradiated surrounding. Due to the fact that there is a kinetic energy gradient of the particles in the expanding wave, the particles pile up at the boundary at different times depending on their velocities. The presence of the energy gradient originates from the plasma gradient. When the pulse impinges on the surface the central portion of the irradiated spot experiences the most intense part of the Gaussian intensity profile of the pulse. The annular region of the spot experiences the least intense part. Therefore, the greatest density of ionizations will be in the centre and the least will be at the edge; between these two extremes is a gradient that follows the Gaussian intensity profile. Since the most intense part of the beam is at the centre these particles acquire the greatest velocities. They move the greatest distance as they move radially from high pressure to low pressure. This substantial motion of the central particles results in the formation of a crater.

Multiple-pulse structures are explained in the same way as the single pulse: plasma gradient produces energy gradient of particles which expand and pile up at the cold boundary. Plasma electrons relax approximately 1 ps after the pulse and the laser repetition rate produces the second pulse 1 ms after the first. Plasma has completely relaxed by the time the subsequent pulse arrives, therefore there is no plasma-laser interaction in the multiple-pulse regime. Structural differences between the single and multiple pulses are attributed to the difference in the plasma geometry. Plasma is produced within the skin depth of a material, therefore since the first pulse morphed the surface, the skin

depth of the second pulse follows the single pulse structure. Although the geometry of plasma is different, the density gradient is the same since the pulse is the same and there is no laser-plasma interaction. Particles in the hydrodynamic wave are reflected by the crater walls forcing them back into the crater where they solidify to form the internal structures.

Asymmetrical features of all structures are attributed to field enhancement caused by under and overcritical plasma densities. During the pulse the material is ionized and becomes greater than the critical density for intrinsic and N-type silicon. The high density of conduction electrons permits using a metal spheroid approximation to silicon. Based on the fact that the plasma frequency exceeds the laser frequency and on the electric field boundary conditions, field enhancement occurs along the direction of the electric field. Due to the greater field, and thus greater intensity experienced by particles along the electric field, there is greater absorption resulting in enhanced features. On the other hand for P-type, a dielectric spheroid is used. Plasma frequency is less than the laser frequency and enhancement occurs orthogonal to the field.

## 5.2 Future work

There is still much to be understood about the mechanism that drives the motion of material in the single pulse case. All of the data presented in Chapter 3 shows a smooth crater formation with a surrounding raised ring. Hence, the theory presented in this thesis was based on melting, and the hydrodynamic motion of the molten material was stated to be responsible for the structure. Evidence for this theory was collected only from SEM and AFM images, there was no data collected during the laser-matter interaction. Information about the trajectories taken by the particles in the hydrodynamic wave would be helpful in understanding if the ring is produced by the solidification of an expanding wave or possibly by re-deposition of removed material. Pump-probe experiments to collect images of the expansion and or removal of material would also be helpful to gain information about the mechanisms of formation of the single pulse and ultimately multiple-pulse structures. Measuring the reflectivity of the laser affected spot over time enables the determination of the melt thickness.

Although there is no explosive removal of material that can be observed by SEM, it does not necessarily mean that no matter has been removed from the surface. For instance electrons, ions, neutral species may be removed [36, 37]. Depending on the fluence, the electrostatic potential between the ionized electrons and the positive lattice

ions may exceed the binding energy of the lattice resulting in the emission of ions [14]. A diagnostic method for determining the ablation threshold is to perform the structuring experiment within a time of flight mass spectrometer and simultaneously measuring the signal of emitted particles [36]. Below the ablation threshold there will be no detected particles, therefore the onset of emission is considered the threshold. Knowledge of the ablation threshold may modify the theory presented in this thesis if it is found that the threshold, under the conditions used, is within the fluence range used. This would mean that there are other mechanisms of material modification besides melting; for instance phase explosion and or void formation may need to be considered.

Images of the hydrodynamic expansion and or material removal may be acquired via pump-probe experiments [38]. The pump is the beam that induces a change in the material and the less intense probe is used to retrieve information about the modification by detection with a camera. The probe is specifically developed to be below any modification threshold so that it solely acts to probe the affected area. A beam splitter divides the primary laser beam into two beams: pump and probe to ensure that they are identical. Often the beam splitter will separate the laser so that most of the intensity goes to the pump. Sometimes the intensity will be equally split and one half of the beam will be frequency doubled. The optics will be set up so that only the frequency doubled portion will be reflected into the setup and the remainder will be removed. Thus, frequency doubling one half ensures that the probe will be significantly less intense than the pump. The beam path of the probe is chosen to be longer than the pump and it is controlled so that different time delays are created. Controlling delays allows for collection of images depicting the formation of the structure. Using shadowgraphy, time resolved images of the generation of a shockwave and plasma expansion or hydrodynamic expansion can be retrieved.

The reflectivity of the molten material oscillates due to the reverberation of the melt front between the different impedances of the air-surface and liquid-solid interfaces. By multiplying the velocity of sound by the period of reverberation, the approximate melt thickness is acquired [39]. Accuracy of the melt thickness may be useful for performing simulations such as molecular dynamics simulations to track the motions of individual particles.

The two-temperature model equations 3.10 - 3.14 can be used to calculate the minimum fluence that equates plasma density to the critical density. This fluence would correspond to the threshold for observing the overcritical behaviour in intrinsic and N-type silicon. Theoretical calculations could be performed to determine the fluence required

to make the plasma density of P-type reach the critical density. Thus, the threshold for the onset of overdense behaviour as well as the end of underdense behaviour would be known. Equations 3.10 - 3.13 could be modified so that fluence instead of intensity would evolve with time and space.

# Bibliography


[1] T.H.R. Crawford and H.K. Haugen. Sub-wavelength surface structures on silicon irradiated by femtosecond laser pulses at 1300 and 2100 nm wavelengths. *Applied Surface Science*, 253:4970–4977, 2007.

[2] Claudia Wu Shrenik Deliwala Eric Mazur Tsing-Hua Her, Richard J. Finlay. Microstructuring of silicon with femtosecond laser pulses. *Applied Physics Letters*, 73:1673–1675, 1998.

[3] Jorg Kruger and Wolfgang Kautek. Ultrashort pulse laser interaction with dielectrics and polymers. *Advanced Polymer Science*, 168:247–289, 2004.

[4] C. Hnatovsky E. Simova R.S. Taylor P.B. Corkum D.M. Rayner P.P. Rajeev, M. Gertsvolf and V.R. Bhardwaj. Transient nanoplasmonics inside dielectrics. *Journal of Physics B: Atomic, Molecular and Optical Physics*, 40:S273–S282, 2007.

[5] Ming Zhou Tommaso Baldacchini, James E. Carey and Eric Mazur. Superhydrophobic surfaces prepared by microstructuring of silicon using a femtosecond laser. *Langmuir*, 22:4917–4919, 2006.

[6] D. Pisignano A. Athanassiou E. Stratakis R. Cingolani P. Tzanetakis V. Zorba, L. Persano and C. Fotakis. Making silicon hydrophobic: wettability control by two-lengthscale simultaneous patterning with femtosecond laser irradiation. *Nanotechnology*, 17:32343238, 2006.

[7] D.S. King R.R. Cavanagh and J.C. Stephenson. Dynamics of nonthermal reactions: Femtosecond surface chemistry. *Journal of Physical Chemistry*, 97:786–798, 1993.

[8] James E. Carey Cynthia M. Friend Michael A. Sheehy, Luke Winston and Eric Mazur. Role of the background gas in the morphology and optical properties of laser-microstructured silicon. *Chemical Materials*, 17:3582–3586, 2005.

[9] Danny Perez and Laurent J. Lewis. Molecular-dynamics study of ablation of solids under femtosecond laser pulses. *Physical Review B*, 67:67–82, 2003.

[10] M. Shen E. Mazur C.H. Crouch, J.E. Carey and F.Y. Genin. Infrared absorption by sulfur-doped silicon formed by femtosecond laser irradiation. *Applied Physics A*, 79:1635–1641, 2004.

[11] B. Luther-Davies E.G. Gamaly, A.V. Rode and V.T. Tikhonchuk. Ablation of solids by femtosecond lasers; ablation mechanism and ablation thresholds for metals and dielectrics. *Physics of Plasmas*, 9:949–957, 2004.

[12] Rafael R. Gattass and Eric Mazur. Femtosecond laser micromachining in transparent materials. *Nature Photonics*, 2:219–225, 2008.

[13] K-A Th Thoma D.P. Korfiatis and J.C. Vardaxoglou. Conditions for femtosecond laser melting of silicon. *Journal of Physics D: Applied Physics*, 40:6803–6808, 2007.

[14] E.G. Gamaly. The physics of ultra-short laser interaction with solids at non-relativistic intensities. *Physics Reports*, 508:91–243, 2011.

[15] R.W. Boyd. *Nonlinear Optics*. Academic Press, Burlington, MA, 3rd edition, 2008.

[16] P. Meynadier-M. Perdrix G. Petite B. Salle, O. Gobert and A. Semerok. Femtosecond and picosecond laser microablation: ablation efficiency and laser microplasma expansion. *Applied Physics A*, 69:381–383, 1999.

[17] S. Nolte-F. von Alvensleben A. Tunnermann B.N. Chichkov, C. Momma. Femtosecond, picosecond, and nanosecond laser ablation of solids. *Applied Physics A*, 63:109–115, 1996.

[18] M.F. Becker D.Y. Sheng, R.M Walser and J.G. Ambrose. Heterogeneous nucleation of damage in crystalline silicon with picosecond 1.06m laser pulses. *Applied Physics Letters*, 39:99, 1981.

[19] P.M. Fauchet and A.E. Siegman. Surface ripples on silicon and gallium arsenide under picosecond laser illumination. *Applied Physics Letters*, 40:824, 1982.

[20] J.E. Sipe H.M. van Driel and Jeff F. Young. Laser-induced periodic surface structure on solids: a universal phenomenon. *Physical Review Letters*, 49:1955–1958, 1982.

[21] J. Reif-M. Bestehorn O. Varlamova, F. Costache. Self-organized pattern formation upon femtosecond laser ablation by circularly polarized light. *Applied Surface Science*, 252:4702–4706, 2006.

[22] D. Wolfframm-A. Tempel M. Henyk, N. Vogel and J. Reif. Femtosecond laser ablation from dielectric materials: Comparison to arc discharge erosion. *Applied Physics A*, 69:355–358, 1999.

[23] J. Reif F. Costache, M. Henyk. Ripples revisited: non-classical morphology at the bottom of femtosecond laser ablation craters in transparent dielectrics. *Applied Surface Science*, 186:352–357, 2002.

[24] J.M. Liu. Simple technique for measurements of pulsed gaussian-beam spot sizes. *Optics Letters*, 7:196–198, 1982.

[25] G.C. Weatherly-H.K. Haugen A. Borowiec, M. Mackenzie. Transmission and scanning electron microscopy studies of single-femtosecond laser-pulse ablation of silicon. *Applied Physics A*, 76:201–207, 2003.

[26] F. Baset K. Popov L. Ramunno J-M Guay, A. Villafranca and V.R. Bhardwaj. Polarization-dependent femtosecond laser ablation of poly-methyl methacrylate. *New Journal of Physics*, 14:2–17, 2012.

[27] P.W. Milonni and J.H. Eberly. *Laser Physics*. John Wiley & Sons, Inc., Hoboken, New Jersey, 2010.

[28] Thornton Ernest Glover. Hydrodynamics of particle formation following femtosecond laser ablation. *Journal of the Optical Society of America B*, 20:125–131, 2003.

[29] Ying-Tung Chen Ampere A. Tseng and Kung-Jeng Ma. Fabrication of high-aspect-ratio microstructures using excimer laser. *Optics and Lasers in Engineering*, 41:827–847, 2004.

[30] J.M. Auerbach P. Lee K.R. Manes, V.C. Rupert and J.E. Swain. Polarization and angular dependence of 1.06 $mu$m laser-light absorption by planar plasmas. *Physical Review Letters*, 39:281–284, 1977.

[31] B.L. Kapeliovich S.I. Anisimov and T.L. Perel'man. Electron emission from metal surfaces exposed to ultrashort laser pulses. *Sov. Phys.-JETP*, 39:375–377, 1974.

[32] W.E. Schiesser and G.W. Griffiths. *A Compendium of Partial Differential Equation Models*. Cambridge University Press, Cambridge, 2009.

[33] M. Blackman M.N. Alam and D.W. Pashley. High-angle kikuchi patterns. *Proceedings of The Royal Society of London A*, 221:224–241, 1954.

[34] T. Yamazaki Y. Takahashi T. Fuyuki, H. Kondo and Y. Uraoka. Photographic surveying of minority carrier diffusion length in polycrystalline silicon solar cells by electroluminescence. *Applied Physics Letters*, 86:262108(1–15), 2005.

[35] Timothy H. Gfroerer. *Encyclopedia of Analytical Chemistry*. John Wiley & Sons, Ltd, Chichester, 2000.

[36] Mengqi Ye and Costas P. Grigoropoulos. Time-of-flight and emission spectroscopy study of femtosecond laser ablation of titanium. *Journal of Applied Physics*, 89:5183–5190, 2001.

[37] Wayne A. Weimer. Plasma emission from laser ablation of the high-temperature superconductor $yba_2cu_3o_7$. *Journal of Applied Physics*, 52:2171–2173, 1988.

[38] J. Yang X. Wang N. Zhang, X. Zhu and M. Wang. Time-resolved shadowgraphs of material ejection in intense femtosecond laser ablation of aluminum. *Physical Review Letters*, 99:167602(1–4), 2007.

[39] L.V. Seleznev D.V. Sinitsyn A.F. Bunkin V.N. Lednev A.A. Ionin, S.I. Kudryashov and S.M. Pershin. Thermal melting and ablation of silicon by femtosecond laser ablation. *Journal of Experimentla and Theoretical Physics*, 116:347–362, 2013.